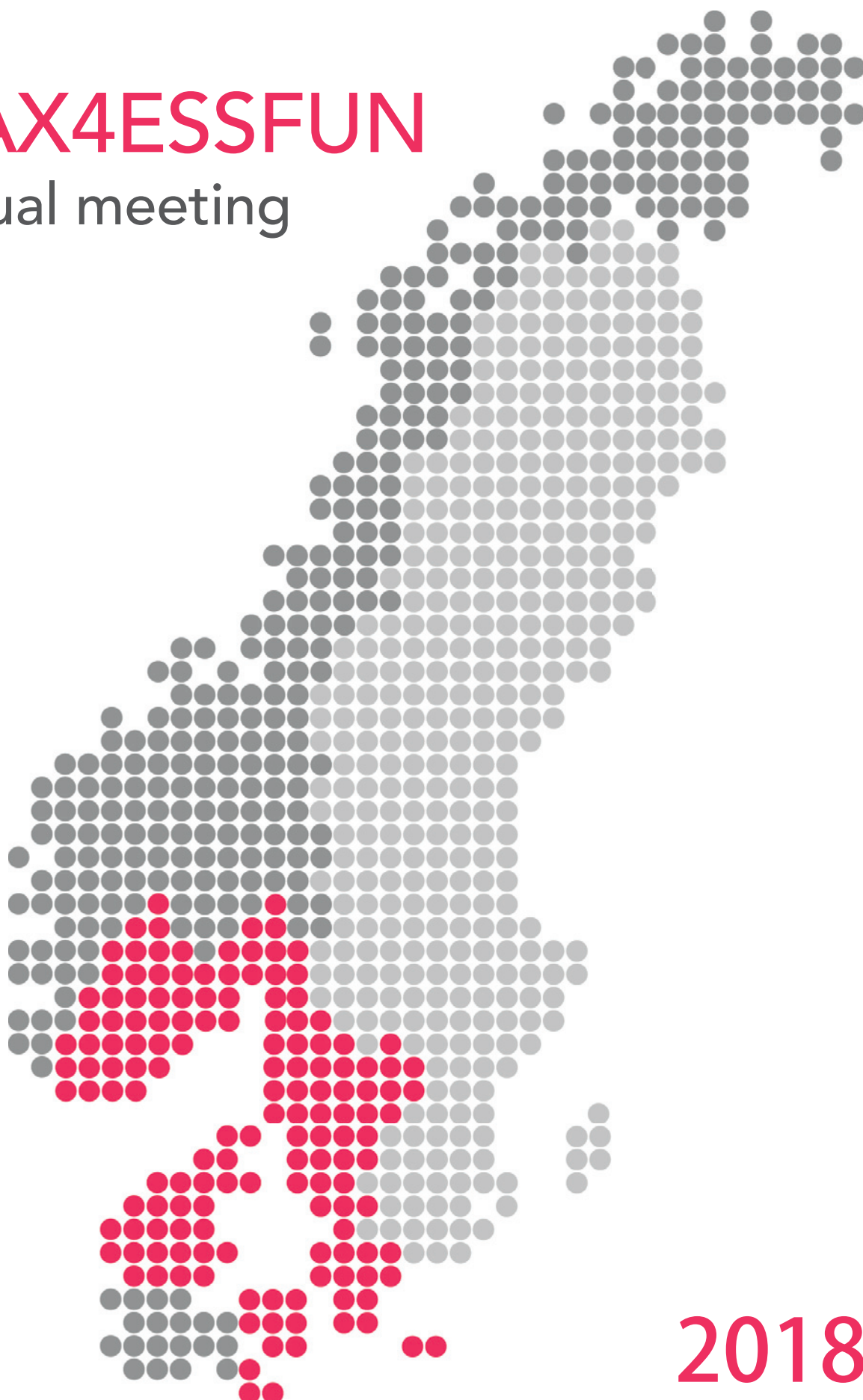


MAX4ESSFUN

annual meeting



2018

Interreg

Öresund-Kattegat-Skagerrak
European Regional Development Fund



EUROPEAN UNION



**ESS & MAX IV:
Cross Border
Science and Society**

MAX4ESSFUN Annual Meeting 2018 Poster Magasin



LUND
UNIVERSITY



CHALMERS
UNIVERSITY OF TECHNOLOGY



**UNIVERSITY OF
GOTHENBURG**



MALMÖ UNIVERSITY



UiO • University of Oslo

Technical University of Denmark



**EUROPEAN
SPALLATION
SOURCE**



LABORATORY



AARHUS UNIVERSITET

programme	2
Anja Schmidt-Christensen	5
Antoni Kowalski	6
Christian Rein	7
Dan Krska	8
Deepak Jain	9
Di Lu	10
Dirk Müter	11
Frederik Gjørup	12
Georgios Kalantzopoulos	13
Giovanni Fevola	14
Hazel Reardon	15
Jonatan Wårdh	16
José Xavier Sierra Trujillo	17
Karin Sahlin	18
Kim Krighaar Rasmussen	19
Kaare Bjerregaard-Andersen	20
Mariam Andersson	21
Monica J Emerson	22
Neelima Kandula	23
Nicolai André Brogaard Riis	24
Rasmus Meland Knudsen	25
Ryan Oliver	26
Scott Mazurkewich	27
Tiago Ramos	28
Tuan Nguyen	29
Wolfgang Knecht	30
List of participants	31

Programme

12 March 2018

12:00 Lunch

12:50 Welcome and introduction by Kell Mortensen

13:00 *Moderator: Ulf Olsson*

NanoMAX - The Hard X-ray Nanoprobe at MAX IV by Ulf Johansson, MAX IV

- Probe Deconvolution for Enhanced X-ray Fluorescence Maps by Tiago Joao Cunha Ramos, DTU.
- Monitoring zinc levels in biological samples using synchrotron X-ray fluorescence imaging by Deepak Jain, LU.
- Bio-sample preparation platform for synchrotron X-ray techniques by Sandra Cuellar-Baena, LU

14:00 *Moderator: Ulf Olsson*

Reflectometry (FREIA/ESTIA) by Artur Glavic, ESS/LU

- Neutron reflectometry from solid-liquid interfaces by Marité Cardenas, Malmö U
- Relaxation pathways in a kinetically trapped, spontaneously polarized molecular glass by Andrew Cassidy, AU
- Self-organized magnetic nanoparticles by Elisabeth Josten, FZ-Jülich

15:00 Coffee break

15:30 *Moderator: Kajsa Paulsson*

Introduction to neutron Imaging by Robin Woracek, ESS

- Imaging microstructures and phase changes by Luise Theil Kuhn, DTU
- Applications to bone-metal implant interfaces by Sophie Le Cann, LU
- Imaging with polarized neutrons by Michael Korning Sørensen, DTU
- Summary by Robin Woracek, ESS

16:30 *Moderator: Kajsa Paulsson*

Neutron Spectroscopy (BIFROST) by Kim Lefmann, KU

- Quantum fluctuations on a hyperkagome lattice by Lise Ørdu Sandberg, KU
- Better background correction: Modelling multiple scattering and background from neutron sample environment by simulation and experiment by Mads Bertelsen, KU
- Why are we looking at magnetic "stripes" in superconductors and what are they? by Sonja Holm-Dahlin, KU

17:30 *Moderator: Kajsa Paulsson*

X-ray Absorption Spectroscopy and its implementation at Balder beamline by Konstantin Klementiev, MAX IV

- X-waste: XANES analysis of waste products for sustainable phosphorus management in agriculture by Nadia Glæsner, postdoc KU
- X-ray absorption and neutron diffraction studies of low dimensional magnetic systems by Mariusz Kubus, DTU

18:30 Poster session and time for networking

19:00 Dinner

13 March 2018

08:00 Breakfast

08:30 *Moderator: Gregers Rom Andersen*

Femto-second spectroscopy - The European XFEL and ultrafast measurements by Martin Meedom Nielsen, DTU

- Tracking Photoconversion with Femtosecond X-ray Scattering and Spectroscopy by Kasper Skov Kjær
- Time-resolved X-ray Absorption Spectroscopy of Copper Zinc Tin Sulfide Nanoparticles by Christian Rein

09:30 *Moderator: Gregers Rom Andersen*

MX by Uwe Mueller & Thomas Ursby, MAX IV

- Synchrotron serial crystallography (SSX), an opportunity for room temperature structure determination of proteins by Anastasya Shilova, MAX IV Laboratory
- Structural investigation of chondroitin/dermatan sulfate biosynthetic enzymes by Emil Tykesson, LU
- Structural determination of an ancient aquaporin by Florian Schmitz, GU

10:30 Coffee Break

11:00 *Moderator: Luise Theil Kuhn*

Introduction to neutron macromolecular crystallography by Esko Oksanen, ESS

- Neutron crystallography in structure-based drug design by Dr. Zoë Fisher, ESS
- Deuterium labelling for neutron crystallography by Katarina Koruza, LU
- Optimising crystal size for triose phosphate isomerase by Vinardas Kelpas

12:00 *Moderator: Luise Theil Kuhn*

SAXS and XPCS - The CoSAXS project at MAX IV by Tomás Plevelic & Ann Terry, MAX IV

- Opportunities of XPCS at MAX IV by Anders Madsen, X-FEL
- Acoustic levitation and SAXS to investigate concentrated protein solutions by Pernille Sønderby, DTU
- Formation kinetics of Poly-Ion complexes studied by time-resolved SAXS by Matthias Amann, UiO
- Summary and Perspectives by Ulf Olsson, LU

13:00 *Short summary by Kell Mortensen*

13:05 Lunch



UiO • University of Oslo



UNIVERSITY OF GOTHENBURG



Technical University of Denmark

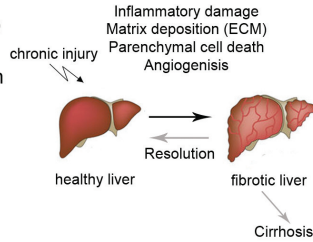


Introduction

Formation and remodeling of the extracellular matrix (ECM) is critical during wound healing and scar formation but excessive connective tissue formation, as seen in fibrosis, can be detrimental and lead to organ failure.

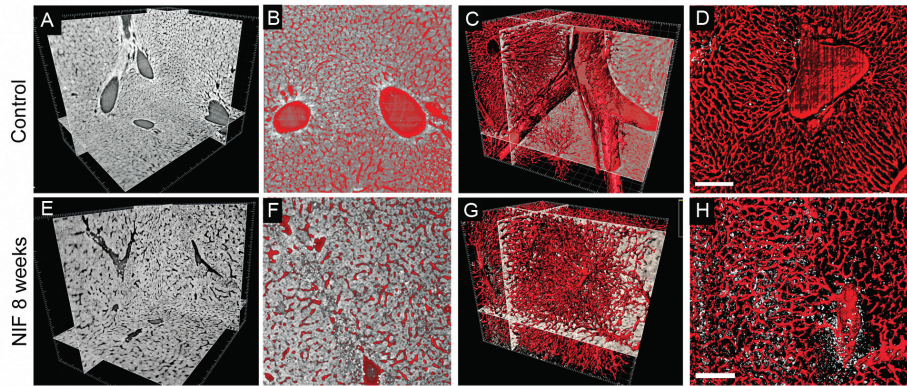
Besides massive ECM accumulation, fibrosis also involves the formation of new vessels (angiogenesis) and the establishment of abnormal angio-architecture of the liver.

We have recently developed a spontaneous animal model, the NIF mouse, that recapitulates the process of persistent



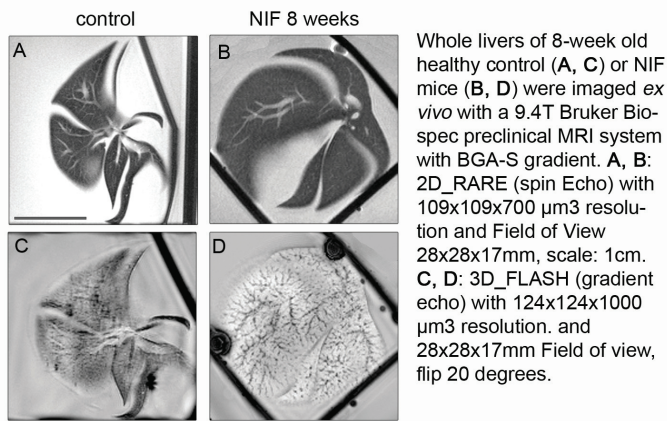
inflammation leading to tissue remodeling and fibrosis that is commonly observed in human fibrotic disorders (1). Current noninvasive clinical and pre-clinical imaging systems are unable to access the spatial resolution domain to reliably detect fibrosis in its early stages, when the process could potentially be stopped or reversed. That grand challenge requires the ability to perform multimodal and multitechnique imaging across all length and time scales. Here we apply label-free synchrotron radiation and Magnetic Resonance Imaging (MRI) with Optical imaging modalities and Histology.

FIG.1 SYNCHROTRON-BASED X-RAY TOMOGRAPHY



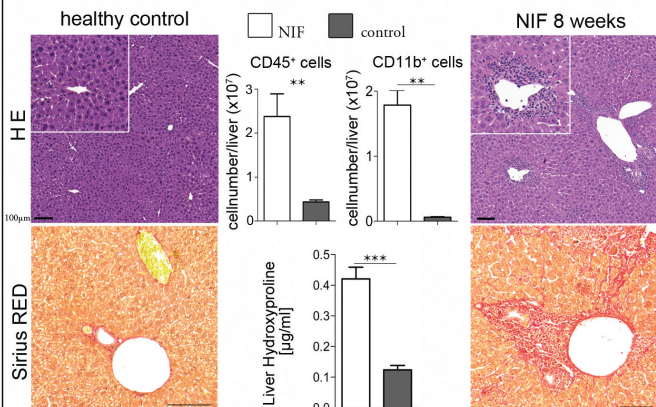
Synchrotron X-ray CT experiments were conducted at the Swiss Light Source (SLS) on the TOMCAT-X02DA Beamline using Paraffin-embedded left lateral liver lobes of 8-week old control (A-D) or NIF mice (E-H). A monochromatized X-ray energy of 21 keV is set in conjunction with a sample-to-source distance of 190mm. Zoom 20x, effective Pixel size 0,32 x 0,32 μm^2 . Tomographic projections were phase-retrieved and CT reconstructed using the Paganin Algorithm. Image stacks were further analyzed using Imaris 9.1 (Bitplane). Shown image size is 567 x 567 x 691 μm (A,C,E,G). A: Orthoslicer view of original CT Reconstruction B: Additional channel (red) was added by inverting black and white values. C: surface rendering of red channel. D: thin 3D slice (normal shading), nuclei (inflammation) in white. Scale bar: 100 μm

FIG.2 MAGNETIC RESONANCE IMAGING (MRI)



Whole livers of 8-week old healthy control (A, C) or NIF mice (B, D) were imaged *ex vivo* with a 9.4T Bruker Biospec preclinical MRI system with BGA-S gradient. A, B: 2D_RARE (spin Echo) with 109x109x700 μm^3 resolution and Field of View 28x28x17mm, scale: 1cm. C, D: 3D_FLASH (gradient echo) with 124x124x1000 μm^3 resolution, and 28x28x17mm Field of view, flip 20 degrees.

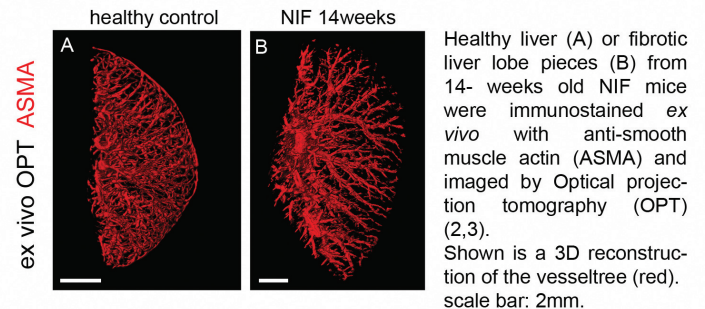
FIG.4 HISTOLOGY AND FACS



Chronic inflammation and fibrosis in the liver of 8 week old NIF mice. Liver sections from 8-week old NIF mice display accumulation of inflammatory cells in areas surrounding the hepatic portal tracts (Hematoxylin and Eosin; HE). Numbers of CD45⁺CD11b⁺ myeloid cells are significantly increased in livers of NIF mice, analyzed by FACS. Extensive fibrosis is illustrated by liver sections stained by Sirius RED and Hydroxyproline content (1)

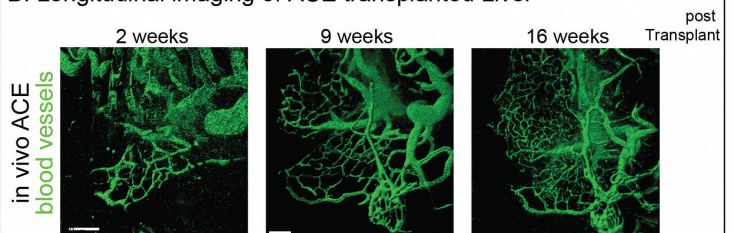
FIG.3 OPTICAL IMAGING MODALITIES: OPT AND ACE

A: Fibrosis leads to abnormal angio-architecture of the liver



Healthy liver (A) or fibrotic liver lobe pieces (B) from 14-week old NIF mice were immunostained *ex vivo* with anti-smooth muscle actin (ASMA) and imaged by Optical projection tomography (OPT) (2,3). Shown is a 3D reconstruction of the vessel tree (red). Scale bar: 2mm.

B: Longitudinal imaging of ACE transplanted Liver



E13 embryonic livers were transplanted into the anterior chamber of the mouse eye (ACE) and imaged repeatedly at indicated time points post transplantation by high resolution 2-Photon microscopy (4). Blood vessels visualized by iv injection of Angiosense 680. (green). Scale bar: 50 μm .

SUMMARY

Advances in the elucidation of the biology of fibrosis, combined with improved technologies for assessment will provide a comprehensive framework for design of antifibrotics and their analysis in well-designed clinical trials.

	synchrotron	MRI	OPT
field of view	0,7 x 0,7 x 0,7 mm ³	28 x 28 x 17 mm ³	ca. 25 x 25 x 25mm ³
resolution	0,32 x 0,32 x 0,32 μm	125 x 125 x 1000 μm	ca. 30 μm
scan time	5 min	1h 30min	15-20min
data size	ca. 25Gb	5Mb	ca. 300Mb

REFERENCES

- Fransen Pettersson N et al., *PLoS One* 2015; 2. Sharpe J et al., *Science* 2002; 3. Alantantalo T et al., *Nature methods* 2007
- Schmidt-Christensen A et al., *Diabetologia* 2013.

Time-resolved X-ray Absorption Spectroscopy of Copper Zinc Tin Sulfide Nanoparticles

Christian Rein¹, Mariana Mar Lucas¹, Kristoffer Haldrup², Asbjørn Moltke², Jens Uhlig³, Jens Wenzel Andreasen¹

1 - DTU Energy, Technical University of Denmark, Risø, Denmark.
2 - DTU Physics, Technical University of Denmark, Lyngby, Denmark.
3 - Lund University, Lund, Sweden.

Introduction

Photovoltaic processes of the earth abundant and non-toxic $\text{Cu}_2\text{ZnSnS}_4$ (CZTS) absorber material in 3. generation solar cells can be investigated by time resolved X-ray absorption spectroscopy (TR-XAS) using a synchrotron-based X-ray source and synchronized laser excitation (pump-probe method). Such experiments require high quality CZTS [1] stabilized as a nanoparticle (NP) ink as a model system, which is also applicable for low-cost up-scalable roll-to-roll (R2R) printing.

CZTS

Kesterite structured CZTS has the best performance when the composition is Cu-poor and Zn-rich [2] within a small region on the phase diagram (figure 1), which reduces the probability for detrimental secondary phases [3]. Theoretical work has also shown that absorber materials with this composition will contain Cu-vacancies responsible for a p-doping of the semiconducting CZTS [2].

Upscaling solar cell fabrication using CZTS requires the material to be synthesized as inks for R2R printing. Oleylamine (OLA) is commonly used as ligands during hot inject synthesis to stabilize CZTS NPs (figure 2-4) [4].

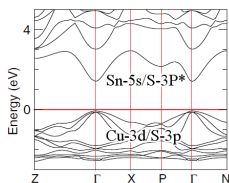


Figure 5: Band diagram of CZTS (kesterite) [9].

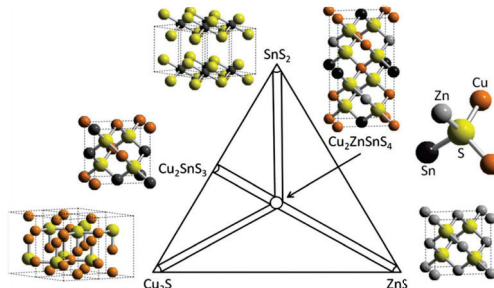


Figure 1: The pseudoternary phase diagram with the kesterite phase and other secondary phases along with their crystal structures [8].

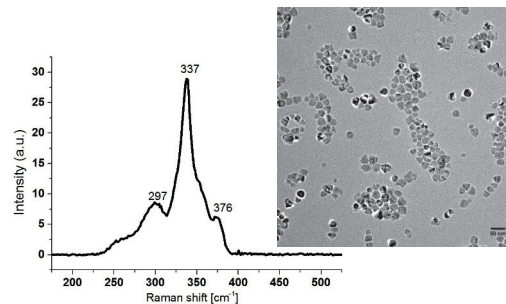


Figure 2: left – Raman spectroscopy data for OLA-coated CZTS NPs. Peaks indicate kesterite structure with no detectable signs of secondary phases. Right – TEM image.

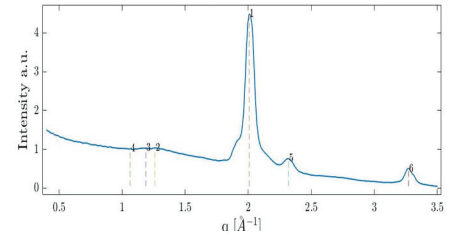


Figure 3: X-ray diffraction data showing the 112-peak for OLA-coated CZTS NPs. Using the Scherrer equation on the FWHM of the 112-peak we estimate the size of the CZTS crystals to be 13-17 nm.

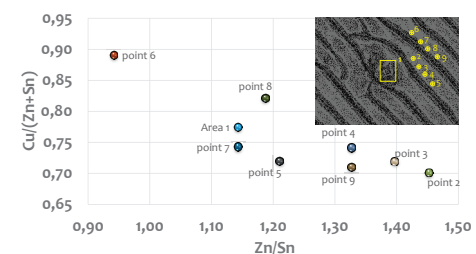


Figure 4: EDX data for OLA-coated CZTS NPs. Insert – SEM image of the samples areas on a dropcasted sample.

Probing photoexcited CZTS with TR-XAS

Upon absorbing a photon ($E_{\text{photon}} > 1.5$ eV) an electron is excited from the Cu-3d/S-3p* state (valence band) to the Sn-5s/S-3p* state (conduction band, Fig. 5), and photocarrier generation, localization and recombination occurs on the fs-, ps- and ns-scale, respectively [5-7]. Localization reduces mobility of charges and it is therefore important to know on what atoms these localizations occur in order to improve the efficiency of the CZTS absorber. By using TR-XAS (Fig. 6) the fate of the charge carriers in the photoexcited CZTS is interrogated at both the Cu and Zn K-edges. We have modelled the expected change in XAS near the Cu-edge for both hole and electron trapping, and is currently comparing it to experimental data (Fig 7).

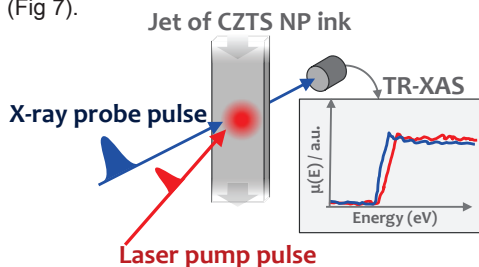


Figure 6: Schematic representation of the pump-probe scenario for the time-resolved x-ray absorption spectroscopy (TR-XAS).

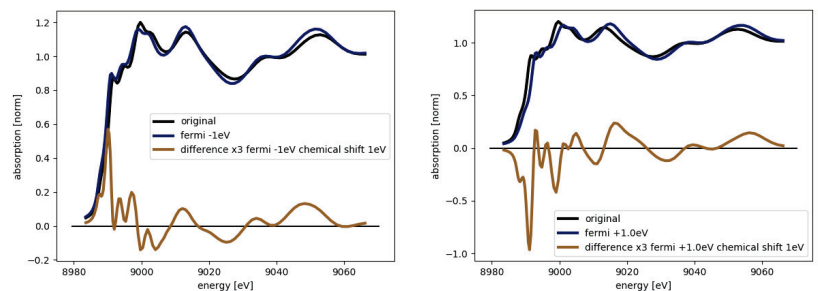


Figure 7: Models of Cu-edge XAS change upon photoexcitation.

REFERENCES:

- (1) Ahmad, R., et al., *Cryst. Eng. Comm.*, 17, 6972–6984, 2015.
- (2) Bourdais, S. et al., *Adv. Energy Mater.*, 1502276, 2016.
- (3) Jung, H. R. et al., *Electron Mater. Lett.*, 12, 139–146, 2016.
- (4) Guo, Q., *J. Am. Chem. Soc.* 2009, 131, 11672–11673, 2009.
- (5) Phuong, L. Q. et al., *Appl. Phys. Lett.*, 231902, 2014.
- (6) Hempel, H. et al., *J. Appl. Phys.*, 120, 175302, 2016.
- (7) Okano, M. et al., *Phys. Status Solidi B*, 252, 219–224, 2015.
- (8) Du, H., et al., *J. Appl. Phys.* 1151, 173502, 2014.
- (9) Paier J. et al., *Phys. Rev. B*, 79, 115126, 2009.

The degradation of plant biomass provides an important source of energy for many microorganisms, and enzymes involved in these processes can be extremely relevant for industrial applications¹. One microbial strategy for degradation of this biomass is the use of enzymes that feature multiple catalytic domains in the same peptide, and one genus of bacteria which utilizes this strategy for plant biomass degradation is *Caldicellulosiruptor*¹. The characterization of a novel multicatalytic xylanase (GH10)/glucuronoyl esterase (CE15) enzyme produced by *C. kristjanssonii*, ADQ41707.1, is the focus of this work. This work also investigates the relevance of multiple carbohydrate binding domains within this large protein, and how they affect the overall activity of the enzyme. Through investigations of this and similar multicatalytic enzymes, it should be possible to create improved enzyme cocktails for industrial biomass degradation.

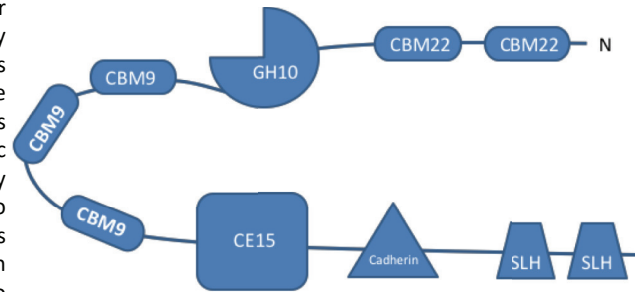


Figure 1: Graphical representation of the domain order of ADQ41707.

CE15 Domain

- Activity shown using both benzyl glucuronate and allyl glucuronate as substrates (Figure 2)
- Limited activity was seen on methyl glucuronate, no activity was seen against methyl galacturonate (data not shown)
- Benzyl glucuronate was the more preferred substrate
- Nearly three-fold increase in k_{cat} seen on the benzyl glucuronate substrate at 40°C (Figure 2C)
- CE15 domain displayed a melting temperature of 77°C (Figure 3), in line with *C. kristjanssonii* growth conditions

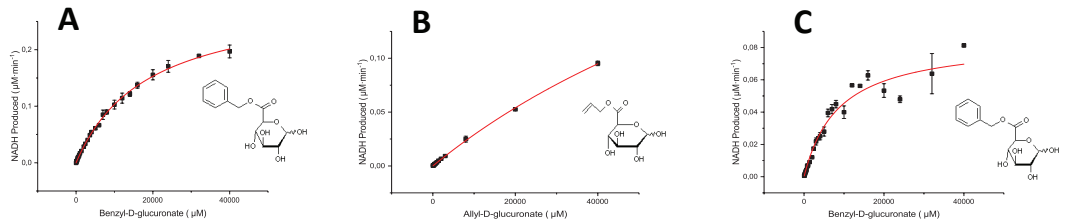


Figure 2: Activity of the CE15 domain with different model substrates. Activity is shown against benzyl glucuronate at room temperature (A), allyl glucuronate at room temperature (B) and benzyl glucuronate at 40°C (C).

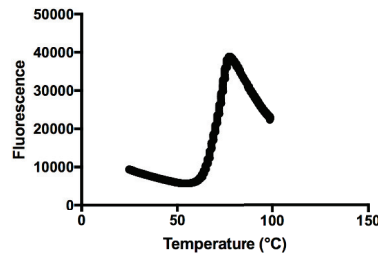


Figure 3: Melting temperature determination of the CE15 domain as determined by a SYPRO Orange fluorescence assay.

Table 1: Kinetic parameters of the activity of the CE15 domain in various conditions as measured in a continuous plate reader assay.

Condition	K_m (mM)	k_{cat} (min^{-1})
22°C, Benzyl Glucuronate Substrate	18,5 ± 0,6	1,18
22°C, Allyl Glucuronate Substrate	125 ± 11	1,56
40°C, Benzyl Glucuronate Substrate	8,6 ± 0,9	3,4

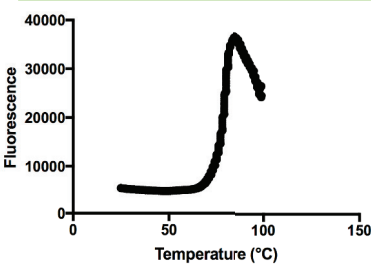


Figure 4: Melting temperature determination of the GH10 domain with both CBM22s as determined by a SYPRO Orange fluorescence assay

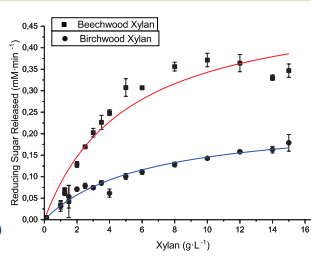


Figure 5: Activity of 50nM GH10 domain acting on both birchwood and beechwood xylan, measured at 65°C.

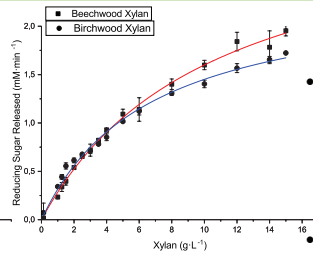


Figure 6: Activity of 500nM CBM22-CBM22-GH10 domain acting on both birchwood and beechwood xylan, measured at 80°C.

Table 2: Kinetic parameters of the xylanase domain acting on xylan substrates as measured using the DNS assay.

Construct	Substrate	Temperature	K_m ($\text{g}\cdot\text{L}^{-1}$)	k_{cat} (s^{-1})
GH10	Birchwood Xylan	65°C	6,2 ± 0,8	80
GH10	Beechwood Xylan	65°C	5,1 ± 0,7	173
CBM22-CBM22-GH10	Birchwood Xylan	80°C	20,4 ± 0,4	80
CBM22-CBM22-GH10	Beechwood Xylan	80°C	10,5 ± 0,7	110

GH10 Domain

- The GH10 domain displays xylanase activity when tested against both birchwood and beechwood xylan with an optimal temperature of 65°C (Figure 5)
- The CBM22-CBM22-GH10 truncation has lower xylanase activity, but an optimal temperature of 80°C (Figure 6)
- pH optimum of approximately pH 7, similar to that of the CE15 domain (data not shown)
- The CBM22-CBM22-GH10 truncation shows a melting temperature of 82°C (Figure 4), in line with the growth conditions of the source organism

Future Direction

- Crystallography of individual domains
- Overall structure determination using small angle x-ray scattering (SAXS)
- The binding affinities of the carbohydrate binding modules (CBMs) will be determined separately
- The “boosting” effect of the multicatalytic architecture will be investigated

References

- Brunecky, R., Alahuhta, M., Xu, Q., Donohoe, B., Crowley, M., Kataeva, I., Yange, S., Resch, M., Adams, M., Lunin, V., Himmel, M., Bomble, Y. Science 2013, 342, 1513-1516

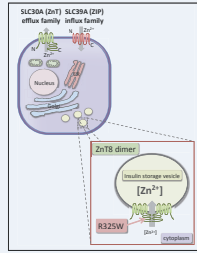
Synchrotron based studies shedding light on membrane proteins: Tapasin and Zinc Transporter ZNT8

Deepak Jain, Dorota Focht, Michael O'Malley, Jens Lagerstedt*, Kajsa M Paulsson*

Zinc transporter 8 (ZNT8)

Introduction

- Diabetes today has reached epidemic proportions and it sets in when the endocrine pancreas that is the pancreatic beta cells do not produce enough insulin to meet the bodies demand.
- Insulin in the pancreatic beta cells is stored as insulin hexamers, which are bound centrally to zinc. In beta cells, zinc is actively transported through the zinc transports-Znts.
- The presence of polymorphism (either R or W at residue 325), confers either increased or decreased risk of developing diabetes.
- Interestingly human subjects carrying truncating variants of the protein have 65 % reduced risk of developing T2D .



OBJECTIVE

- To measure zinc levels in islets of transgenic mice expressing truncated zinc transporter protein i.e. ZNT8.

RESULTS



Figure 1: Expression of Znt8 in pancreatic beta cell line. LSM images of INS-1 cells after transient transfections with full length ZNT8-mCherry construct. Insulin (green, Figure 1a) ZNT8 (red, Figure 1b) and both insulin and ZNT8 (Figure 1c) . ZNT8 co-localizes with insulin as indicated by yellow colour.

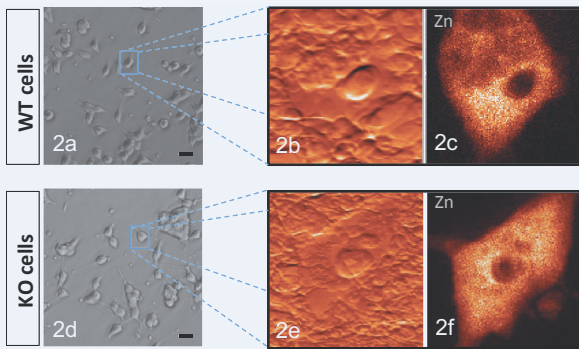


Figure 2: CRISPR knockout of Znt8 in beta cell line leads to redistribution of Zn in beta cells. X-ray fluorescence images of cultured cells including non-modified INS1 beta cells (Figure 2a,b and c) and INS1 cells lacking one or two alleles of the Znt8 gene (Figure 2d,e and f), were grown on silicon nitride membrane, fixed, air dried and scanned for zinc levels at Argonne National Laboratory. Zinc was localized in small pockets in wild type cells compared to uniform redistribution in KO cells.

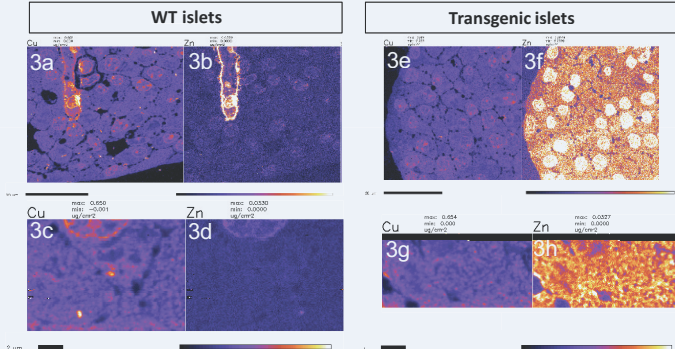


Figure 3: X-ray fluorescence images showing zinc level distribution in islets of control (Figure 3a,b,c and d) and transgenic animals (Figure 3e,b,c and d). Quantification of zinc levels indicating higher zinc levels in transgenic animals compared to control. Experiment was performed at Bionanophore, Argonne National laboratory.

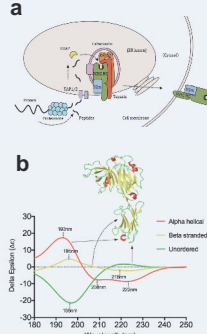
CONCLUSION

- X-ray fluorescence studies show that homozygous deletion of ZNT8 in pancreatic beta cells lead to redistribution of zinc, which in contrast is localized to specific pockets in wild type cell. Further transgenic heterozygous animals expressing truncated ZNT8 protein revealed higher zinc levels in islets compared to the control. Higher zinc levels in islets of transgenic animals could potentially explain the protective phenotype against development of type-2 diabetes.

Tapasin

Introduction

- Major histocompatibility complex type I (MHC-I) antigen presentation is a key mechanism for cells to communicate their internal environment to CD8+ immune cells.
- CD8+ T cells distinguish normal 'self' peptides from abnormal viral or tumour peptides, and respond by killing infected cells.
- Prior to display at the cell surface on MHC-I, endogenous antigens must be loaded into the MHC-I binding cleft by the peptide loading complex (PLC).
- Tapasin is a key molecule in the PLC, and one of its main functions is determining which peptides are presented by MHC-I at the cell surface. This mechanism is still poorly understood.
- To understand the function of different domains of tapasin protein i.e. Tpn₈₇, Tpn₂₇₀, and Tpn₃₉₂, protein of indicated size were purified and subjected to SRCD analysis.



OBJECTIVE

- To analyze the thermostability and secondary structure structure of Tpn₈₇, Tpn₂₇₀, and Tpn₃₉₂ using SRCD.

RESULTS

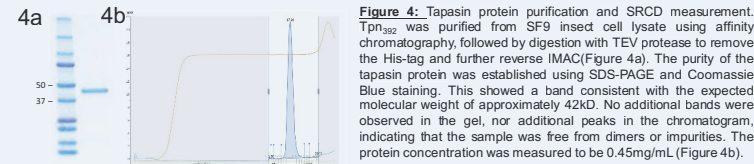


Figure 4: Tapasin protein purification and SRCD measurement. Tpn₃₉₂ was purified from SF9 insect cell lysate using affinity chromatography, followed by digestion with TEV protease to remove the His-tag and further reverse IMAC (Figure 4a). The purity of the tapasin protein was established using SDS-PAGE and Coomassie Blue staining. This showed a band consistent with the expected molecular weight of approximately 42kD. No additional bands were observed in the gel, nor additional peaks in the chromatogram, indicating that the sample was free from dimers or impurities. The protein concentration was measured to be 0.45mg/mL (Figure 4b).

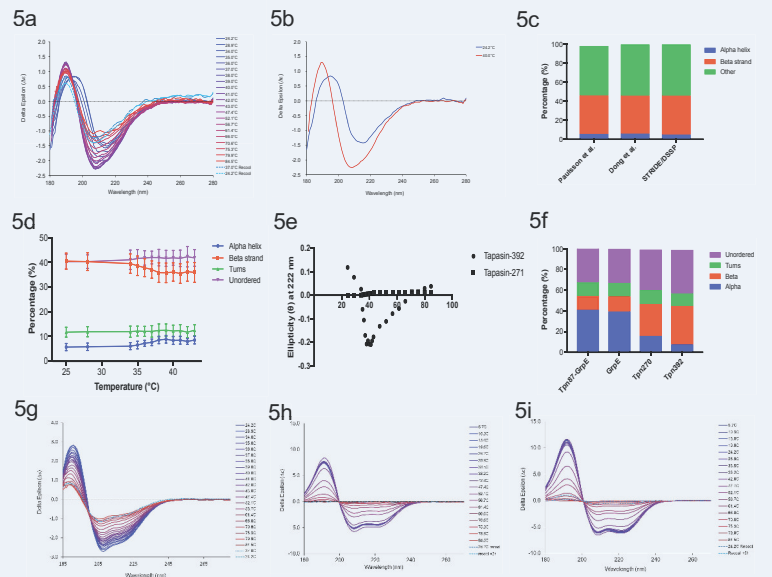


Figure 5: Thermal denaturation of Tpn₃₉₂. Protein undergoes progressive unfolding at higher temperature (Figure 5a). Structural transition occurs around physiological temperature i.e. 37°C, resulting in higher alpha-helical content (Figure 5b). The secondary structure composition of Tpn₃₉₂ at 24°C matches existing crystal structure and theoretical data (Figure 5c). Secondary structure estimation with Dichroweb quantified this transition, indicating a small but significant decrease in beta strand content from 41% to 37% (p<0.0001) between 24°C and 37°C, with a concomitant increase in alpha helices from 6% to 8% (p<0.0001) (Figure 5d). The transition was also confirmed by measuring the absorbance at 222nm, a signature peak of alpha helical proteins. This indicates a peak in alpha helical content around 37-40°C (Figure 5e). Percentage distribution of secondary structure in different domains of tapasin protein (Figure 5f). A temperature scan of Tpn₂₇₀ showed a more typical ellipsoidal shape, with a slightly more alpha-helical structure than Tpn₃₉₂ (Figure 5g). Tpn₈₇ was revealed to have a highly alpha helical structure (Figure 5h), due mainly to the contribution of the GrpE fusion protein (Figure 5i), which has a very similar curve.

CONCLUSION

- This study shows that tapasin, a key molecule involved in MHC class I antigen presentation undergoes a conformational transition in Tpn₃₉₂ at 37°C, which seems to be unique to the full-length protein.

FUNDING

This project was funded by MAX4ESSFUN.



REFERENCES

- Chen, M., Stafford, W. F., Diedrich, G., Khan, A. and Bouvier, M. (2002). A characterization of the luminal region of human tapasin reveals the presence of two structural domains. *Biochemistry* 41: 14539–14545.
- Grafodatskaya, D., Choufani, S., Ferreira, J. C., Butcher, D. T., Lou, Y., Zhao, C., Weksberg, R. (2010). EBV transformation and cell culturing destabilizes DNA methylation in human lymphoblastoid cell lines. *Genomics*, 95(2), 73–83.
- Kuznetsova, I. M., Turoverov, K. K., Uversky, V. N. (2004). Use of the Phase Diagram Method to Analyze the Protein Unfolding-Renaturation Reactions: Fishing Out the "Invisible" Intermediates. *Journal of Proteome Research*, 3 (3), 485-494
- Lees, J. G., Miles, A. J., Wien, F., & Wallace, B. A. (2006). A reference database for circular dichroism spectroscopy covering fold and secondary structure space. *Bioinformatics*, 22(16), 1955-1962.
- Li, W., Joshi, M. D., Singhania, S., Ramsey, K. H., & Murthy, A. K. (2014). Peptide Vaccine: Progress and Challenges. *Vaccines*, 2(3), 515–536.



Introduction

Negative ions are fundamentally interesting due to their highly correlated electrons. The photodetachment process of negative ions has been investigated for several decades[1], essentially by measurements of total and differential cross sections where neutral fragments are detected.

Recent activities at Gothenburg University Negative Ion Laser Laboratory (GUNILLA)[2] are:

- A novel electron spectrometer, PEARLS (*Photoelectron Energy- and Angular- Resolved Longitudinal Spectrometer*)[3] has been designed to perform angular resolved spectroscopy of positive and negative ions using synchrotron radiation.
- Investigation of graphene on quartz plate, as a substitute for traditional Indium Tin Oxide (ITO) coated glass, in a neutral particle detector. Experiments shows surprisingly good transparency and less photoelectric effect working in the UV range with photon energy up to 5.5 eV[4].
- Spectroscopy excited states of the Ru⁻ ion. The results will be used for studies of the lifetimes of the excited states using the Double ElectroStatic Ion Ring ExpEriment (DESIREE) at Stockholm University,
- Improvement of the ion yield of the Cs sputter negative ion source at GUNILLA[6].

Spectroscopy of Ru⁻

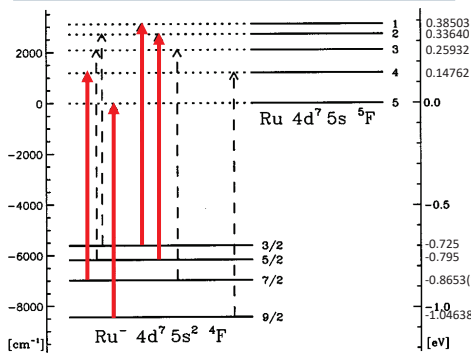


FIG 5. Energy level diagram of Ru⁻ and the Ru ground state. The arrows indicate the allowed detachment thresholds. The red arrows are the transitions of interest, where the binding energies of 2J=9 and 2J=7 levels have been investigated in [5].

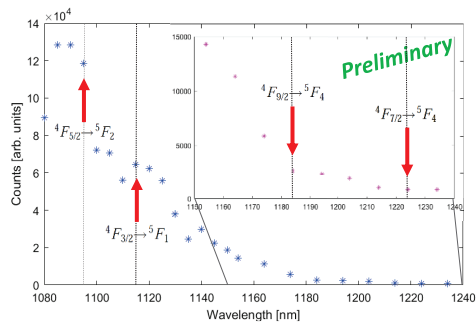


FIG 6. The thresholds behavior for photodetachment of Ru⁻ (J=9, 7, 5 and 3 4F) into the Ru (5F) states.

GUNILLA

The ion beam apparatus at GUNILLA is designed for photodetachment studies using pulsed lasers in a collinear geometry. Following laser interaction, fast neutral atoms are detected as a function of experimental parameters, such as laser wavelength or laser power.

PEARLS

- A merged beams setup.
 - Interaction region of 22 cm.
 - 16 detectors in 4 perpendicular directions.
 - UHV environment of $\sim 10^{-9}$ mbar.
 - especially enhanced photoelectron signal. (important when the photon flux is low, for instance, at synchrotron radiation sites)
- Measurements of the asymmetry parameter β gives information of the amplitudes and relative phases of the emitted electrons.

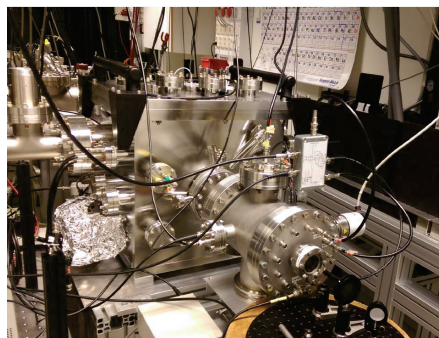
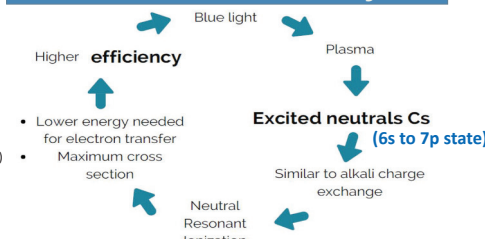


Figure 2. PEARLS shown as part of GUNILLA.

Promotion of the ion yield



Example: Cs (3.9 eV) + hv (Photon) = Cs* (Excited states)
Cu (1.2 eV) + Cs* (2.7 eV) = Cu⁻ + Cs⁺

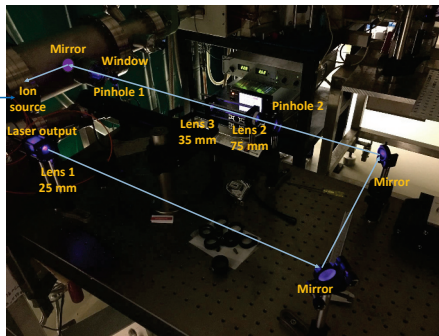


Figure 7. Optical setup for focusing the Ti:Sa laser (10973.2 cm⁻¹) on or close to the surface of the cathode of Cs sputter negative ion source at GUNILLA. A Cs hollow cathode lamp is applied for wavelength calibration.

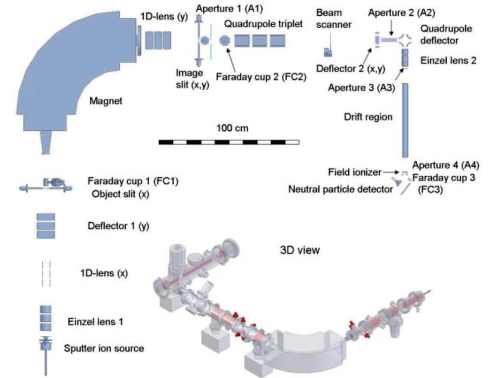


Figure 1. Overview of the ion beam apparatus at GUNILLA.

Graphene vs ITO

ITO coated glass:

- Insufficient transparency above photon energies of 3.6 eV.
- Strong photoelectric effect above photon energies of 4.3 eV.

Graphene:

- 225 to 472 nm, transparency of at least 80%.
- Small photoelectric effect also above photon energies of 4.8 eV.
- Secondary laser induced signals are several orders of magnitude smaller than those from photoelectron process.

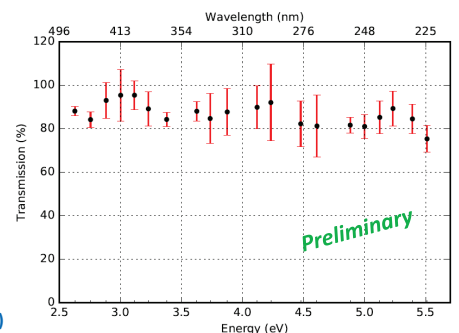


Figure 3. Transmission measurement of graphene in dependence on photon energies. Data shows an overall good transparency of one atomic graphene layer on a quartz glass plate.

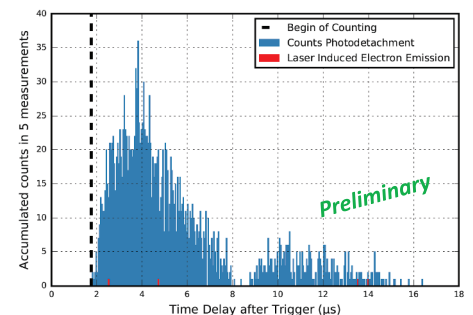
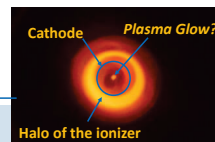


Figure 4. Experiment of the photodetachment and laser induced events at photon energy of 5.51 eV. Five measurements over a range of 15 µs have been accumulated.



Contact

Dr. Di Lu
Department of Physics
University of Gothenburg
Email: di.lu@physics.gu.se
Phone: +46 0730298161

References

1. F. J. Wuilleumier, et al., *J. Electron Spectrosc. Rel. Phenom.* **88-91** (1998) 41-52.
2. C. Diehl, et al., *Rev. Sci. Instrum.* **82** (2011) 053302.
3. O. Windelius, et al., *Nucl. Instrum. Methods Phys. Res. B.* **410** (2017) 144-152.
4. J. Warbinek, "Investigation of the photoelectric effect in graphene and ITO in a neutral particle detector". Bachelor thesis (2018).
5. P. L. Norquist, et al., *Phys. Rev. A.* **59** (1999) 1896-1902.
6. A. Duckworth, et al., *Optics & Laser Tech.* **24** (1992) 39-43.

Acknowledgement

This work was partially supported by MAX4ESSFUND



MULTISCALE MECHANICAL MODELLING OF CHALK

D. Müter¹, K.N. Dalby¹, S. Bruns¹, J. Oddershede², K. Uesugi³, S.B. Skattum⁴, D.K. Dysthe⁴, H.O. Sørensen¹

¹Nano-Science Center, Department of Chemistry, University of Copenhagen, Denmark

²Department of Physics, Technical University of Denmark, Lyngby, Denmark

³Spring-8, Hyogo, Japan

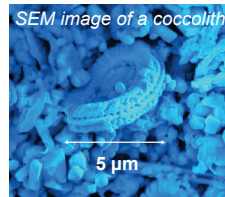
⁴Department of Physics, University of Oslo, Norway

Introduction

Chalk is a highly porous rock formed from the remains of ancient algae (coccolithophores). A large volume of groundwater and hydrocarbon reservoirs are hosted in chalk, thus being able to estimate the mechanical response is important. Here, we demonstrate how to combine ultra-high resolution synchrotron based nanotomography with larger field of view laboratory microtomography to derive meaningful estimates of the mechanical properties of chalk using a multiscale finite element modelling approach.

Chalk Samples

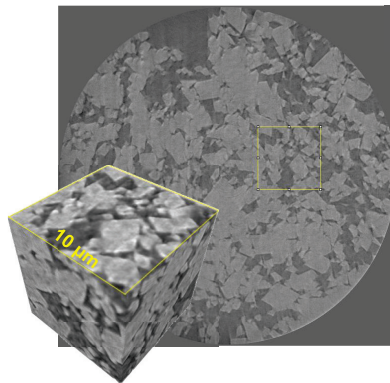
- Chalk samples were taken from core plugs (25 mm diameter) from off-shore drilling.



Nanotomography

- X-ray nanotomography (nanoCT) data were recorded on small chips (~100 μm in size) at beamline BL47XU at Spring-8, Japan with a voxel size of about 40 nm.

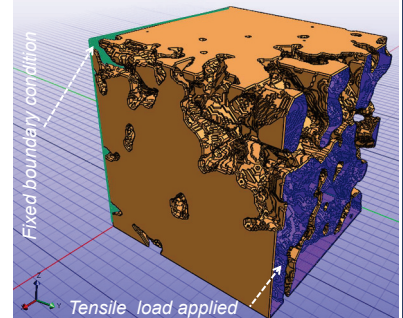
Spring-8, Japan



Mechanical Modelling

- Subvolumes of nanoCT data (6 μm edge length) were segmented, meshed and imported into finite element software (FEBio).
- A tensile testing setup was used to calculate the subvolume's effective Young's modulus, E_{eff} .
- Data point for subvolumes from the same sample were fitted with this empirical equation (n and ϕ_0 as fitting parameters):

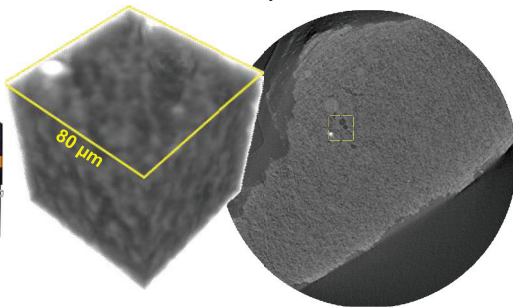
$$E_{eff} = \frac{E^*}{E_0} \left(1 - \frac{\phi}{\phi_0} \right)^n$$



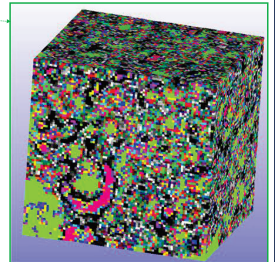
Microtomography

- X-ray microtomography (μCT) data were recorded on chips from core plugs at the Imaging Industry Portal at the Technical University of Denmark with a voxel size of about 1 μm.

DTU Versa Instrument

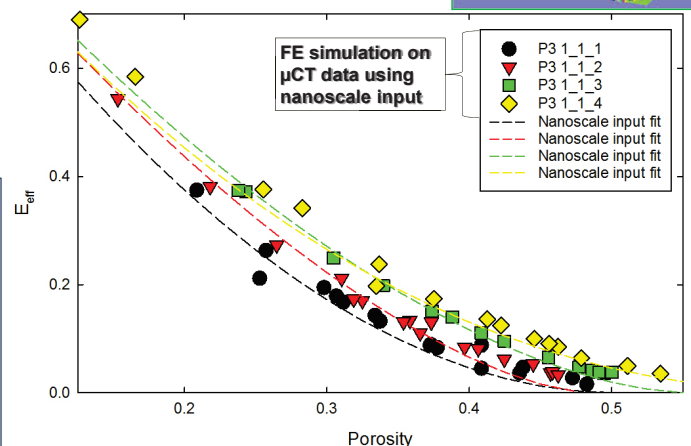


- The nanoscale porosity-elasticity relationship was then used to assign material properties for every voxel in the μCT data.
- Mechanical properties of subvolumes of μCT data (80 μm edge length) were calculated to derive a microscale porosity-elasticity relationship utilizing the results from high-resolution nanoCT.



Outlook: Fracturing in Peridynamics

Peridynamics, similarly to DEM depicts a porous medium as spheres connected by bonds. These bonds can be broken thus allowing for fracturing in the sample. First comparisons between our FEM and peridynamics show good agreement on the elastic properties therefore moving towards fracturing in chalk will be the next step forward.



Conclusions

We have demonstrated how to derive meaningful mechanical properties (Young's modulus) of chalk from X-ray tomography while combining the ultra-high resolution of synchrotron based nanoCT with the larger field of view in laboratory μCT. The results on the microscale are generally similar to the nanoscale input, but for some samples there is a systematic bias towards higher values of E_{eff} . We will investigate this in more detail to produce reliable procedures for upscaling of these results to the centimeter (core-plug) scale and beyond, which should prove very valuable for industrial drilling applications.

Acknowledgements

We thank Mærsk Oil & Gas for providing the samples as well as funding and Innovation Fund Denmark for co-funding via the P³ project. D. M. is grateful for financial support through the ERC via INTERREG

Publications

D. Müter, H. O. Sørensen, D. Jha, R. Harti, K. N. Dalby, H. Suhonen, R. Feidenhansl, F. Engstrøm & S. L. S. Stipp. *Resolution dependence of petrophysical parameters derived from X-ray tomography of chalk*. Appl. Phys. Lett. 105, 043108, 2014

D. Müter, R. Harti, K. N. Dalby, M. Guizar-Sicairos, M. Holler, J. C. da Silva, S. L. S. Stipp, H. O. Sørensen. *Nanoscale mechanical properties of porous materials from ptychographic X-ray imaging*. In preparation.



Novel Experimental Setups for *In Situ* Neutron Diffraction

AARHUS UNIVERSITY

Jakob V. Ahlburg, Frederik H. Gjørup, Mathias Mørch, and Mogens Christensen
Center for Materials Crystallography, Department of Chemistry & iNANO, Aarhus University, Denmark

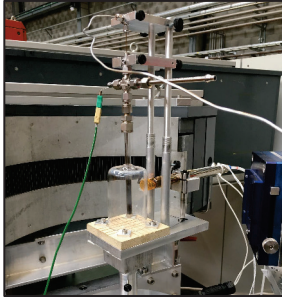
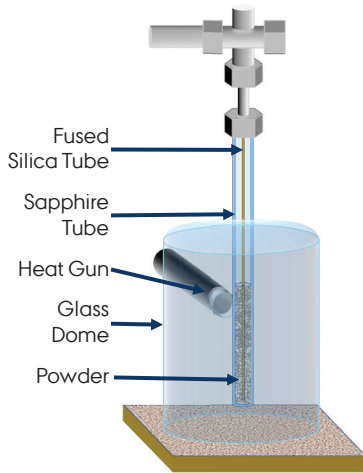
jakob.ahlburg@inano.au.dk - fjgorup@chem.au.dk - mmorch@chem.au.dk - mch@chem.au.dk



Modern synchrotron and neutron sources provide the intensities needed for performing never-before-seen experiments. With the imminent launch of the scattering facilities MAX IV & ESS, it is interesting to explore novel setups that enable new experiments at these sites. X-ray and neutron techniques compliment each other greatly, for instance by utilizing the difference in scattering lengths.

X-ray scattering lengths scale with the number of electrons, which is not the case for neutrons. Neutrons can give a contrast between near-isoelectronic scatterers, for instance the neighbouring Fe and Co. Neutrons also provide information on the magnetic structure and can probe large bulk samples, allowing the study of compacted powders for use in permanent magnets.

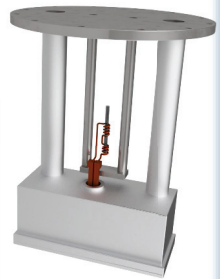
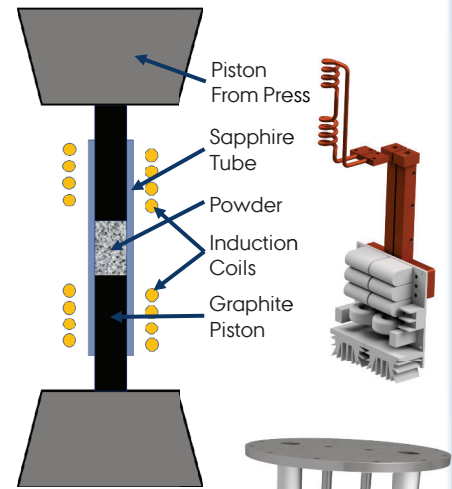
Reduction Setup



In the **reduction setup** 5% H₂ in Ar gas is released through a fused silica tube at the bottom of the sapphire sample holder. The sample is heated with an air gun, to a maximum of ~750 °C.

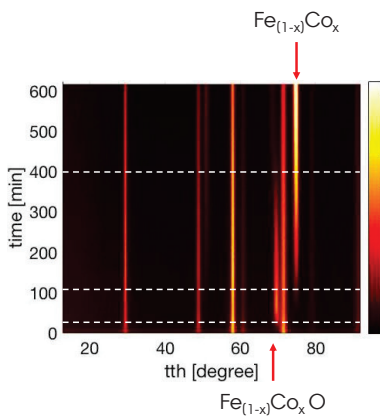
The sapphire tube used in the **induction press setup** can withstand a pressure of 100 MPa. Induction coils will heat the graphite pistons to temperatures of up to 1000 °C. The entire setup will be placed in a vacuum container.

Induction Press Setup



	Reduction Setup	Induction Press Setup
Maximum Temperature	750 °C	1000 °C
Designated Instrument	DMC @ SINQ	POLARIS @ ISIS
Sample Mass	~2 g	~2 g
Heating Rate	>100 K/min	>15K/s
Reaction Gas Option	✓	✓
Pressing Option	✗	✓

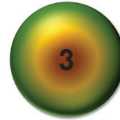
Preliminary Results: Reduction of CoFe₂O₄



Almost all Fe_(1-x)Co_xO has been reduced



Fe_(1-x)Co_xO is further reduced to bcc Fe_(1-x)Co_x



CoFe₂O₄ is partly reduced to Fe_(1-x)Co_xO



Pure CoFe₂O₄ spinel



In situ neutron reduction experiments of magnetic CoFe₂O₄ was performed on DMC at SINQ, varying the temperature and the flow of H₂. The data shown to the left is reduction carried out at 490°C and a 10 ml/min flow of 5 % H₂/Ar. First only the CoFe₂O₄ peaks are visible but this will reduce to Fe_(1-x)Co_xO and further to Fe_(1-x)Co_x. By aiming for a mixture of magnetically hard spinel and magnetically soft metal one can achieve exchange coupling. A possible reaction mechanism is shown to the left.



Georgios N. Kalantzopoulos^{1,*}, Fredrik Lundvall¹, Nils Lau Nyborg Broge², Frederik M Søndergaard-Pedersen²
 Anna Lind³, Bjørnar Arstad³, David S. Wrapp¹, Jacob Becker², Bo Brummerstedt Iversen² and Helmer Fjellvåg¹.

¹Department of Chemistry, University of Oslo, Sem Sælands vei 26, N-0371 Oslo, Norway.

²Center for Materials Crystallography, Department of Chemistry, Aarhus University, Denmark

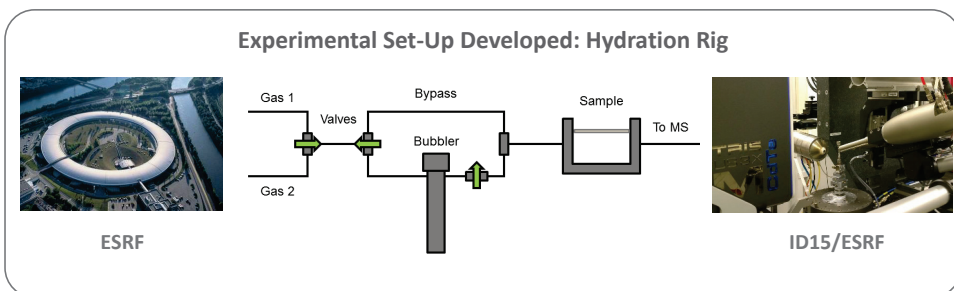
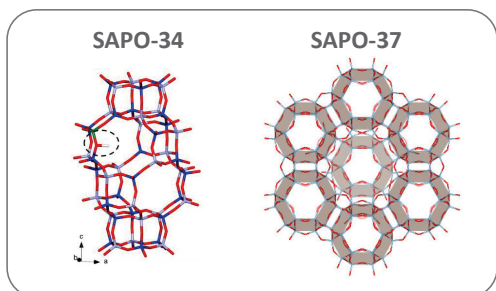
³SINTEF Materials and Chemistry, Forskningsveien 1, N-0314 Oslo, Norway.

*georgiok@smn.uio.no.

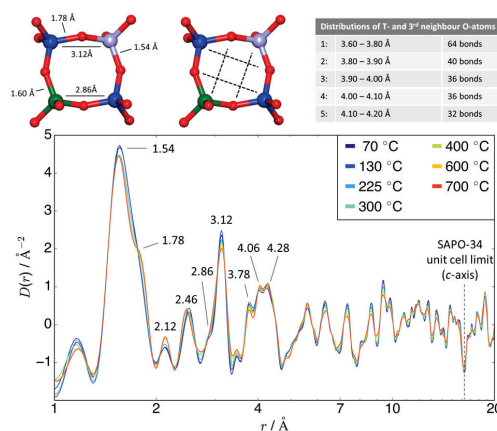
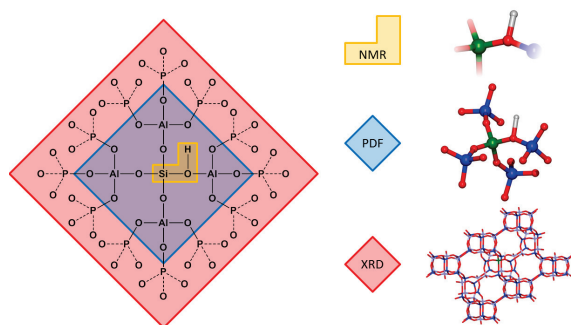


Project Summary

Silicoaluminophosphates (SAPOs) are a special class of zeolites used broadly in industrial processes such as the methanol-to-olefins (MTO) conversion and the isobutene/2-butene alkylation. During **real-life industrial applications** SAPOs are **exposed to humidity**, a critical parameter that promotes structural changes, leading to their **deactivation and consecutively total performance loss**. Although this problem has been known since the early 1990s, the **mechanism governing the local structural transformations that humidity induces** in those materials still remains to be experimentally revealed. This MAX4ESSFUN project focused on **studying in detail these structural transformations in industrially-relevant conditions**. It brought together two groups from the University of Oslo (Helmer Fjellvåg's group) and Aarhus University (Bo Brummerstedt Iversen's group) with extensive complimentary experience in **synchrotron XRD** and **pair distribution function (PDF) analysis**.



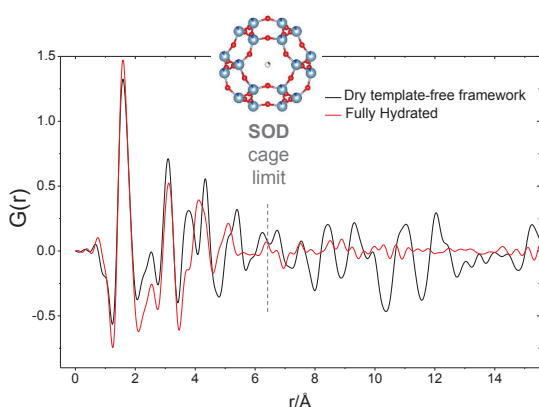
In-situ synchrotron PDF analysis of the local response of the Brønsted acidic site in SAPO-34 during hydration at elevated temperatures¹



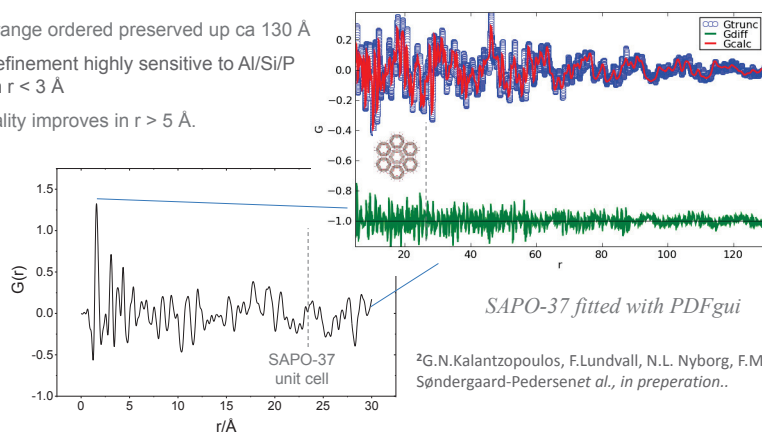
¹In-situ flow MAS NMR and synchrotron PDF analyses of the local response of the Brønsted acidic site in SAPO-34 during hydration at elevated temperatures”, G.N.Kalantzopoulos, F.Lundvall et al. ChemPhysChem, 2018, 19, 519-528.

First SAPO-34 (and SAPO in general) structural model resolved by PDF

In-situ synchrotron PDF analysis of the mechanism leading to the amorphization of SAPO-37 during hydration²



- Long-range ordered preserved up ca 130 Å
- PDF refinement highly sensitive to Al/Si/P ratio in $r < 3 \text{ \AA}$
- Fit quality improves in $r > 5 \text{ \AA}$.



²G.N.Kalantzopoulos, F.Lundvall, N.L. Nyborg, F.M. Søndergaard-Pedersen et al., in preparation..

Combined Scattering and Fluorescence Mapping of Kesterite Precursors at the NanoMAX Beamline

Tiago Ramos^a, Giovanni Fevola^a, Mariana Mar Lucas^a, Christian Rein^a, Jens W. Andreasen^a

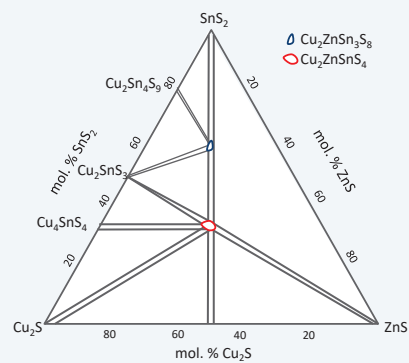
^a Technical University of Denmark – Department of Energy Conversion and Storage, Roskilde, Denmark

Abstract: Materials with the approximate stoichiometry $\text{Cu}_2\text{ZnSnS}_4$ with the crystal structure of the mineral kesterite are currently being investigated as promising materials for thin film solar cells fabrication. Direct imaging, along with chemical analysis, can crucially contribute to assess the quality of the process. This poster presents the results from the obtained fluorescence and scattering maps from a sample of kesterite precursors produced by pulsed laser deposition (PLD). The obtained chemical information was compared with energy dispersive spectroscopy (EDS) measurements previously made on the same sample.

Introduction: Third-generation photovoltaic solar cells are currently under research and development as an attractive technology for cheap and efficient solar energy conversion. This new type of solar cells is characterized by its design (thin films) and by the use of non-toxic and Earth-abundant materials with a potential significant decrease in energy payback time when compared to common silicon-based solar cells.

Kesterite photovoltaics utilizing $\text{Cu}_2\text{ZnSnS}_4$ (CZTS) are one of the promising emerging technologies that have already demonstrated a high absorption coefficient (10^4 cm^{-1}) and a direct band gap of 1-1.5 eV which allows an effective energy absorption in absorber layers of a few microns.

One of the main challenges during the synthesis of CZTS is related with formation of different secondary phases that compromise the operation of this material as a photoelectric converter. The phase diagram below exhibits the narrow confined conditions for the synthesis of the desired $\text{Cu}_2\text{ZnSnS}_4$ phase.

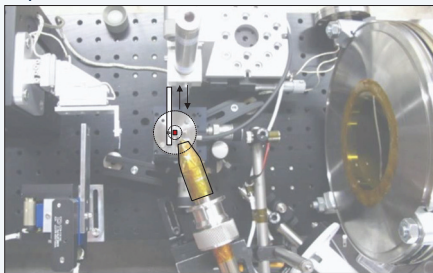


Kesterite Phase Diagram: Quasi-ternary phase diagram of the Cu-Zn-Sn-S system at 400°C. (Olekseyuk, Dudchak & Piskach 2004)

A good understanding of different synthesis methods is therefore essential in order to control the optimal conditions for kesterite formation and improve future thin-film kesterite solar cells.

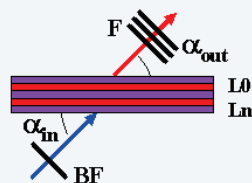
Sample Preparation: A thin film sample of kesterite precursors ($2\text{CuS}:\text{ZnS}:\text{SnS}$) was prepared with pulsed laser deposition (PLD) over a soda-lime glass substrate intercalated with a thin Molybdenum layer.

Experimental Setup: We acquired both fluorescence and scattering maps from a thin film CZTS sample, illuminated by an 10.72 keV X-ray beam at the NanoMAX beamline.

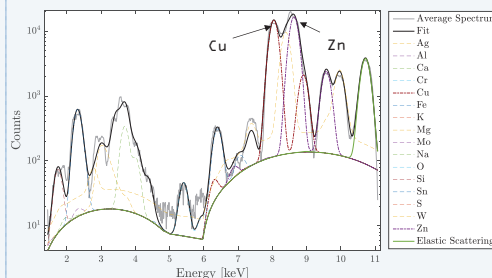


Experimental Setup: X-ray fluorescence data was acquired by a detector placed in transmission mode at approximately 70° from the outgoing beam. Diffraction patterns were acquired simultaneously at the exact same sample positions of the fluorescence measurements.

Data analysis: The acquired fluorescence spectra were processed with PyMca, a dedicated software developed in the European Synchrotron Radiation Facility (ESRF).

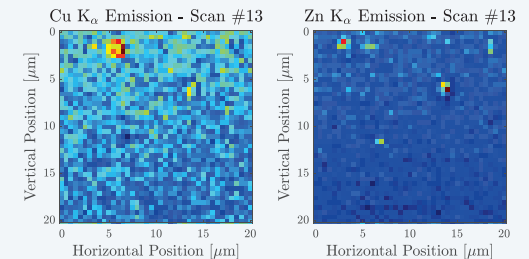


Experimental Setup Definition in PyMca: The introduction of additional information regarding the sample and experimental setup allows the definition of the proper matrix correction coefficients required for quantitative assessment of the precursors mass fractions in the sample.

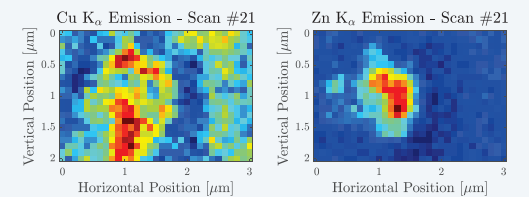


Average Fluorescence Spectrum: The measured spectra presents contributions from the different elements that constitute the kesterite precursors, molybdenum layer and soda-lime glass substrate. An elastic scattering peak and signals from the surrounding equipment can also be observed.

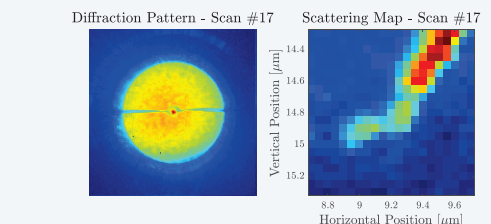
Results: The obtained results allow the identification of several inhomogeneities in the kesterite precursors deposition. The measured stoichiometric ratio between Cu and Zn was found to be in agreement with previous EDS measurements.



Surface overview: A large 20x20 micrometers area was mapped in order to locate hotspots associated with non-uniform precursors distribution. The fluorescence maps above suggest local higher concentrations of Cu and Zn in different sections of the sample that may be related with secondary phases.



Detailed view: A local scan of 3x2 micrometers area was performed in one of the detected hotspots. We believe that the observed structure in the Cu and Zn fluorescence maps is associated with the presence of a droplet on the sample surface with uneven distribution of the CuS and ZnS precursors. Droplet structures on the sample surface of similar dimensions were also observed in SEM images.



Scattering Maps: Scattering maps computed from local integrations of the measured diffraction patterns can provide additional information about the surface morphology and identify possible defects such as cracks that are not visible in fluorescence maps.

Acknowledgements: We would like to acknowledge all the NanoMAX team (Gerardina Carbone, Ulf Johansson, Alexander Björling and Marianne Liebi) for their support during data acquisition and processing. We thank Zdenek Matej and Armando Sole for their assistance with the fluorescence data processing and Stela Canulescu from DTU Photonics for providing the sample and synthesis related information.

Cross Border Study of the Miscibility Gaps in $Mg_2Si_{1-x}Sn_x$

Hazel Reardon^a, Andrey Sizov^b, Lirong Song^a, A. E. C. Palmqvist^b, P. Erhart^b & B. B. Iversen^a

^aCenter for Materials Crystallography, Department of Chemistry & iNANO, Aarhus University, Aarhus, Denmark

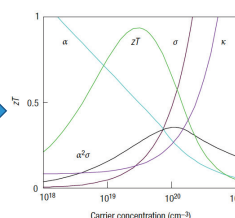
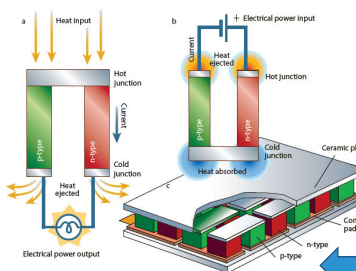
^bChemistry & Chemical Engineering, Chalmers University of Technology, Gothenburg, Sweden

Optimising Thermoelectric

- Thermoelectric materials can convert thermal gradients to electrical potentials, and present a significant opportunity to exploit waste heat produced by industrial effluents streams and in vehicle exhausts (Figure 1).¹ Thermoelectric modules consist of p- and n- type materials, which are assembled in to modules (Figure 2).
- $Mg_2Si_{1-x}Sn_x$ is a commercially relevant material for TE modules.
- The presence of a miscibility gap in $Mg_2Si_{1-x}Sn_x$ has been the subject of much discussion in research on this particular system, and groups at both AU and CUT are probing the known $0.4 \leq x \leq 0.6$ miscibility gap region (former) and a broader region (latter) of the phase diagram.^{2,3}

Aim: To investigate the phase splitting that is observed in $Mg_2Si_{1-x}Sn_x$ solid solutions within the miscibility gap at high temperature.

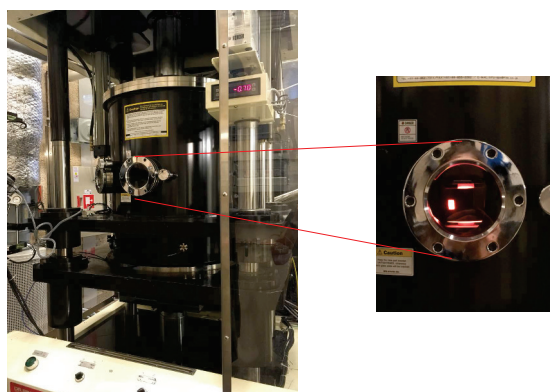
Figure 1 – zT equation and plot of the thermoelectric Figure of Merit (zT) vs. carrier concentration – various material properties must be considered to design the ideal TE material.¹



$$zT = \frac{\alpha^2 \sigma}{\kappa} T$$

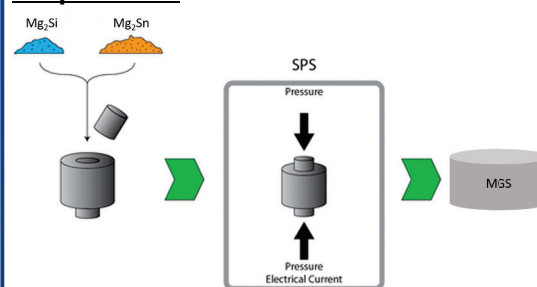
Figure 2 – Representation of the a) Seebeck and b) Peltier thermoelectric effects, and c) the configuration of a TE module.

Spark Plasma Sintering (SPS) Method



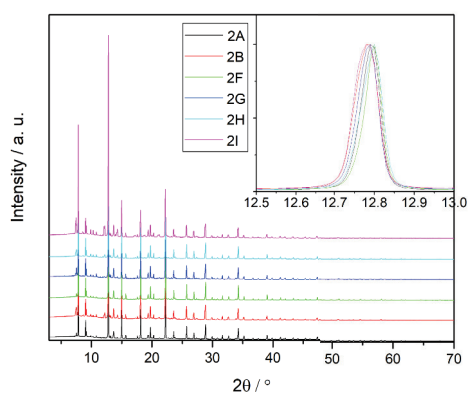
- Compared with conventional densification methods, the complexity and process time of the SPS method is significantly reduced (order of magnitude), making large-scale production feasible.
- Figure shows the SPS press at Chalmers University of Technology, where a synthesis performed as part of the project is in progress.

Preparation



- Mg_2Si and Mg_2Sn was mixed and then packed in to the graphite SPS die. The material was then compressed and heated simultaneously.
- The synthesis parameters were optimized to ensure reproducibility, where the composition, hold time, cooling rate, and temperature were modified independently.

Powder X-ray Diffraction Observations



- Samples were retrieved from the pellets by crushing and then floating the sample in ethanol. Synchrotron data was collected at SPring-8 (Japan) and Rietveld refinements are now in progress in partnership with Chalmers.
- The data reveals that there are some impurity phases in the product, but there is also evidence to suggest that the microstructure of the samples are influenced by the SPS processing method and the conditions employed.

Conclusions and Outlook

- Our understanding of the scale-up and synthesis of the $Mg_2Si_{1-x}Sn_x$ system has been greatly improved by our systematic SPS study; an important step in commercialization of this material.
- The influence of microstructure will be the focus of the next stage of this research, to determine how the thermoelectric properties are affected.
- A stronger collaboration between Chalmers and Aarhus University has been nurtured by this project, and new ventures have been discussed.

References

- G.J. Snyder & E. S. Toberer, *Nat. Mater.*, 2008, **7**, 105; 2. Q. Zhang *et al.*, *J. Phys. D: App. Phys.*, 2008, **41**, 185103; 3. L. Chen *et al.*, *J. Mater. Res.*, 2011, **26**, 3038.

Acknowledgements – HR would like to thank J. Borsson and Andrey Sizov. BBI and HR gratefully acknowledge beamtime at RIKEN BL44B2, Spring-8.

Abstract

We consider electrons in two dimensions with a tunable attractive interaction and a pair-hopping term deriving an effective Ginzburg-Landau theory to study the BCS to BEC crossover. We show that a quantum phase transition from a homogeneous superconducting state, on the BCS side, to a finite momentum superconducting state, on the BEC side, is realized for an arbitrarily weak pair hopping term. At stronger pair-hopping amplitude the continuous quantum phase transition is pushed to a first order transition at finite temperatures.

Pair-Density Wave versus FFLO

It is well established that various coexisting orders, in particular spin- and charge-density wave order, are important components of the cuprate high-temperature superconductors phenomenology. A distinct state where the superconducting order is modulated around a mean of zero has also been discussed, referred to as a pair-density wave (PDW) state. The PDW order is a unidirectional singlet superconducting order that varies in space as $\Delta(\mathbf{r}) = \Delta_{\mathbf{Q}} \cos(\mathbf{Q} \cdot \mathbf{r})$ with \mathbf{r} the center of mass coordinate. It is related to the finite momentum pairing states originally discussed by Fulde-Ferrell and Larkin-Ovchinnikov (FFLO), but in the cuprates believed to arise in a system without spin-population imbalance. This state is suggested to play a significant role for the anomalous suppression of superconductivity in LBCO at 1/8 doping[1] by decoupling CuO_2 layers[2] and may be the mysterious “pseudo-gap state”. Any direct evidence for the state has been missing until very recently.[3, 4] However, there is no clear understanding from microscopics of how such a state would arise.

The present work provides a framework in which an arbitrarily weak “Josephson-interaction” or pair-hopping can destabilize a homogeneous strong coupling superconductor into a PDW state. The goal is that having such a microscopic model for PDW order, more complicated scenarios can be studied including spin and charge order and key experimental signatures can be derived.

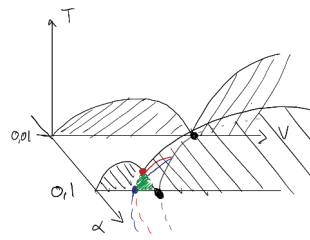


Figure 1: Schematic phase diagram of the pair-hopping model in the BCS to BEC crossover. For small pair-hopping α there is a second order transition through a quantum critical point. For larger α there is tricritical point, indicative of a first order transition.

Model

The aim of this work is to derive a Ginzburg-Landau effective theory for a FF-like PDW state ($\Delta(\mathbf{r}) = \Delta_{\mathbf{Q}} e^{i\mathbf{Q} \cdot \mathbf{r}}$) from a microscopic pair-hopping interaction.

$$H = \int_{\mathbf{r}} \psi_{\sigma}^{\dagger}(\mathbf{r}) \frac{-\nabla^2}{2m} \psi_{\sigma}(\mathbf{r}) - \frac{V}{2} \int_{\mathbf{r}_1, \mathbf{r}_2} T(\mathbf{r}_1 - \mathbf{r}_2) \psi_{\sigma}^{\dagger}(\mathbf{r}_1) \psi_{\sigma}^{\dagger}(\mathbf{r}_2) \psi_{\sigma}(\mathbf{r}_1) \psi_{\sigma}(\mathbf{r}_2) \quad (1)$$

with $T(\mathbf{r}_1 - \mathbf{r}_2) = \delta(\mathbf{r}_1 - \mathbf{r}_2) - \alpha \delta(\mathbf{r}_1 - \mathbf{r}_2 \pm \hat{x} \lambda/2)$ where $\alpha > 0$ describes a pair-hopping interaction, similar to a π -phase Josephson junction.

Through the use of a Hubbard-Stratonovich transformation we can write down the partition function $Z = Z_0 \text{Tr} e^{-\beta F(\Delta)}$ as a sum over a bosonic field Δ

$$F = \frac{1}{\beta} \left(\int_{\mathbf{p}, i\Omega} \Gamma^{-1}(\mathbf{p}, i\Omega) |\Delta(\mathbf{p}, i\Omega)|^2 + \frac{b}{2} \int_{p_1, p_2, p_3} \Delta(p_1) \Delta^*(p_2) \Delta(p_3) \Delta^*(p_1 - p_2 + p_3) \right) \quad (2)$$

$$\Gamma^{-1}(\mathbf{p}, i\Omega) = \frac{T^{-1}(\mathbf{p})}{g} - \int_{\mathbf{k}} G(\mathbf{k} + \frac{\mathbf{p}}{2}, i\omega + i\Omega) G(-\mathbf{k} + \frac{\mathbf{p}}{2}, -i\omega), \quad b = \int_{\mathbf{k}} G^2(\mathbf{k}, i\omega) G^2(-\mathbf{k}, -i\omega).$$

We use this to find the critical temperature T_c and chemical potential μ_c by solving

$$\min_{\mathbf{p}} \Gamma^{-1}(\mathbf{p}, 0) = 0, \quad n = \frac{T}{\text{Vol}} \frac{\partial \ln Z}{\partial \mu} = n_F + n_B, \quad n_B = -\text{Tr} \Gamma \frac{\partial \Gamma^{-1}}{\partial \mu}. \quad (3)$$

where n_F is the free-fermion occupation and n_B the number of bosons (or pre-formed Copper pairs).

Strong coupling limit

In the weak coupling limit $\mu \approx \varepsilon_F, \mu\beta \rightarrow \infty, n_F \gg n_B$ we receive the familiar BCS limit. In strong coupling $\mu < 0, \mu\beta \rightarrow -\infty, n_B \gg n_F$ all fermions are essentially bound up in pairs with mass

$$m_B = 2m \left(1 - \frac{8\pi\varepsilon_A e^{-\frac{\mu}{\varepsilon_A}} \alpha^2}{V} \right)^{-1} \quad (4)$$

(here ε_A is the ultraviolet cut-off). For $\alpha = 0$ we find $m_B = 2m$. For $\alpha > 0$ we find an important correction. In fact, for $\alpha > \frac{\varepsilon_A}{2} (\rightarrow 0 \text{ for } \varepsilon \rightarrow \infty)$ there exists an interaction strength for which the mass diverge, indicating an instability towards a finite momentum, FF, state

$$dV_c = -\frac{2}{W\left(-\frac{\varepsilon_A}{\alpha\varepsilon_A}\right)} \quad (5)$$

where W is the Lambert W function.

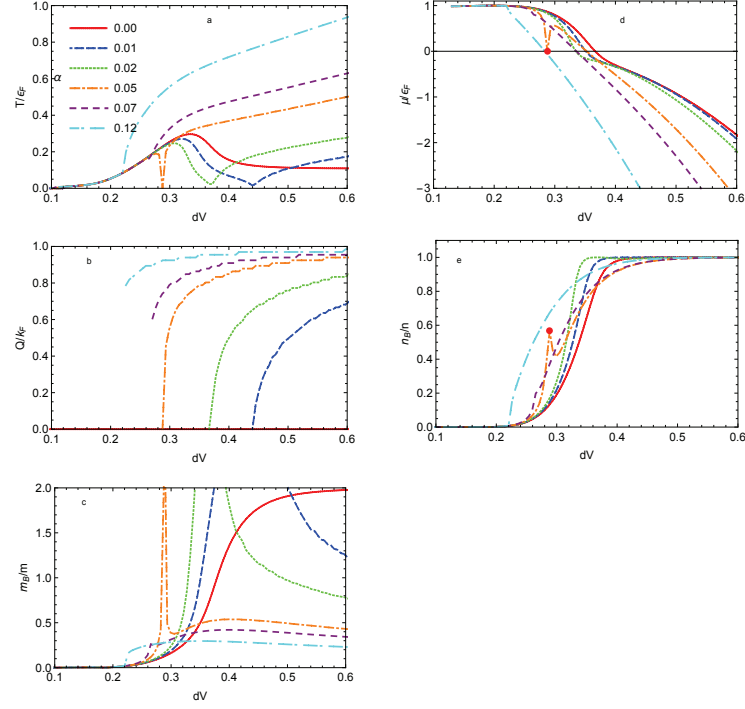


Figure 2: The evolution of T_c, Q, m_B, μ, n_B as a function of interaction strength. Here $\varepsilon_F = 1, \varepsilon_A = 50, \lambda = \frac{2\varepsilon_A}{\sqrt{2}}$ where energy is measured in $\frac{\hbar^2}{m\varepsilon_A}$ and lengths in a . Points indicated by a red dot is not to be trusted and should be omitted.

Results

The main results are shown in Figure 2 for one set of density and λ and a few realizations of α .

- **Fig 2a** For $\alpha = 0$ we see that T_c saturates at strong coupling. However, for small α ($\alpha = 0.01; 0.02; 0.05$) T_c is suppressed when approaching the phase transition to finite Q (Fig 2b).
- **Fig 2b** Onset of finite ordering vector Q . The transition is of second order for small α and first order for bigger α .
- **Fig 2c** The second order phase transition coincides with the divergence of the effective mass.
- **Fig 2d,e** By increasing α we effectively move forward the strong coupling regime. This can be seen from the relative occupation of bosonic degrees of freedom n_B/n (in Fig 2e) accompanied by the onset of negative chemical potential $\mu < 0$ (Fig 2d).
- Note the rather violent behavior at $\alpha = 0.05$. Here the transition to a finite Q state occurs on what would have been the weak coupling side. However, due to the divergent effective mass it is pulled over to the strong coupling side at the critical point, making the critical point inherently strong-coupled.

Relevance to ESS and MAX IV

ARPES and Neutron scattering have been two of the most important probes of the fundamental properties of the cuprate superconductors.

- ARPES has been crucial in mapping out the Fermi surface, the nature of the d-wave gap function, and the strong correlation properties of electronic quasiparticles.

Present work: There are very few ARPES studies of stripe ordered LBCO at 1/8th doping.[5] Here one would have reason to expect more direct evidence for a PDW state, exemplified in Fig.3.

- Magnetic order and magnetic spectra have been intensively studied in the past using elastic and inelastic neutron scattering, including the discovery of striped spin-density wave (SDW) order.[1]

Present work: we expect that there is a subdominant triplet PDW mode $\Delta_{\pi, \pi}$ generated in a system with coexisting PDW and SDW order. This should be studied using using neutron scattering in the superconducting state, also in a magnetic field.

Figure 3: Fermiarc like Fermi surface in a Fulde-Ferrell state.

References

- [1] Tranquada, J. M., et al. "Evidence for stripe correlations of spins and holes in copper oxide superconductors." *nature* 375.6532 (1995): 561.
- [2] Berg, Erez, et al. "Dynamical layer decoupling in a stripe-ordered high-T c superconductor." *Physical review letters* 99.12 (2007): 127003.
- [3] M. H. Hamidian *et al.*, *Nature* 532, 343 (2016).
- [4] S.D. Edkins *et al.*, "Magnetic-field Induced Pair Density Wave State in the Cuprate Vortex Halo", arXiv:1802.04673 (2018).
- [5] R.-H. He *et al.* Energy gaps in the failed high-Tc superconductor $\text{La}_{1.875}\text{Ba}_{0.125}\text{CuO}_4$, *Nat. Phys.* 5, 119 (2009).
- [6] Wårdh J, Granath M. "Effective model for a Supercurrent in a Pair-Density Wave" *Phys. Rev. B* 96, 224503 (2017).

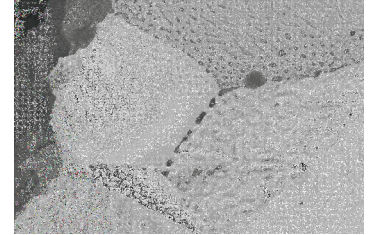
In operando studies of ScYSZ electrolyte supported symmetric solid oxide cell by X-ray Diffraction

J.X. Sierra¹, H. F. Poulsen², P. S. Jørgensen¹, C. Detlefs³, P. Cook³, H. Simons², C. Yildirim³, S. R. Ahl², A. C. Jakobsen², I. Kantor², J. R. Bowen¹
1: Technical University of Denmark (DTU Risø), 2: Technical University of Denmark (DTU Lyngby), 3: ESRF Beamline ID06
jxst@dtu.dk



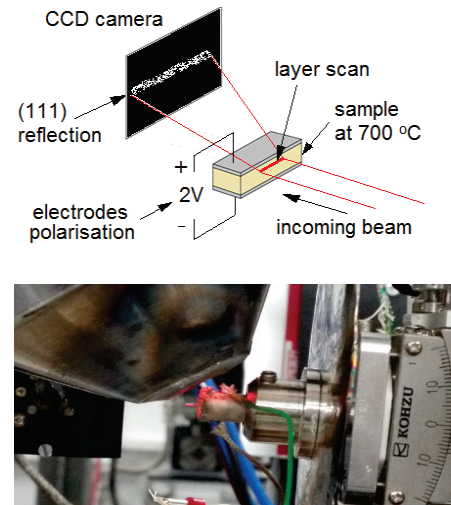
Introduction

Solid Oxide Cells are becoming a promising solution for sustainable and renewable power generation. Scandium doped Ytria Stabilized Zirconia is considered one of the best materials used as electrolyte because of its high ionic conductivity and great mechanical and chemical stability under operating conditions. Oxygen bubble formation at grain boundaries of ScYSZ near the anode/electrolyte interface has been observed as a degradation process when running in electrolysis mode at 800 - 900 °C for 24 - 72 hours at high current densities. X-ray diffraction can provide information about structural evolution at different depths of the cell during operation.

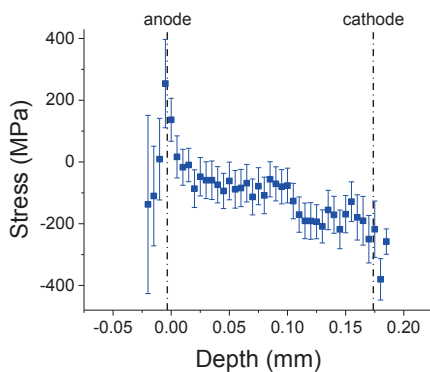


Structural evolution and oxygen bubble formation

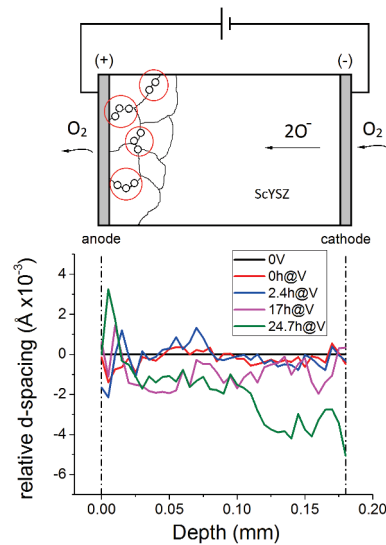
Setup of the synchrotron beamline hutch at ESRF - ID06 Beamline:



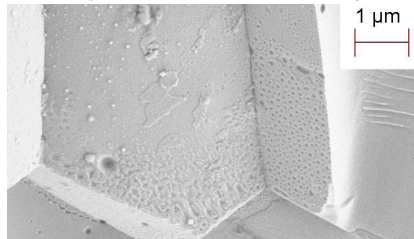
Estimated stress across the cell only from Δd -spacing



Relative d-spacing of (111) diffraction line across the cell and schematic view of the cell polarization and bubbles found.



Oxygen bubble formation in electrolyte close to the anode region

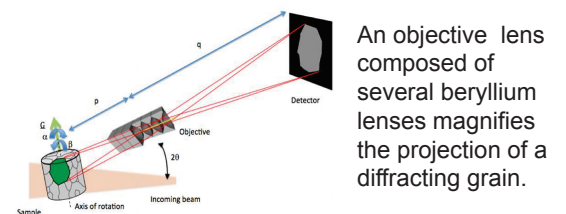


Results

A gradient in d-spacing is observed across the cell after 24 hours. Decrease of d-spacing at the anode/electrolyte region can be associated to the high oxygen pressure build up. Decrease of d-spacing in the cathode/electrolyte region could be related to oxygen deficiency caused by the high cathodic polarization. X-ray microscopy revealed changes in the morphology and strain domains inside one grain after 10 hours running at operating conditions. Snapshots show changes in the internal structure when the current is applied.

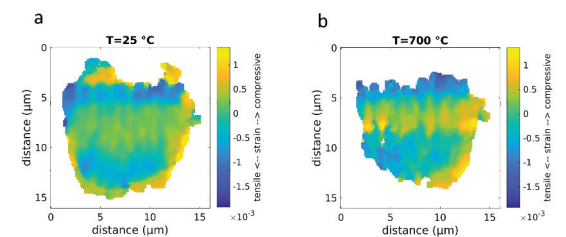
Dark Field X-Ray Diffraction Microscopy

At ID06 beamline we are currently commissioning a dark field microscope, which enables zooming in on mm-sized samples and perform 3D mapping of grains and stresses at a 100 nm scale in regions of 200 μm. This provides unprecedented opportunities for studying microstructural changes in operando materials.

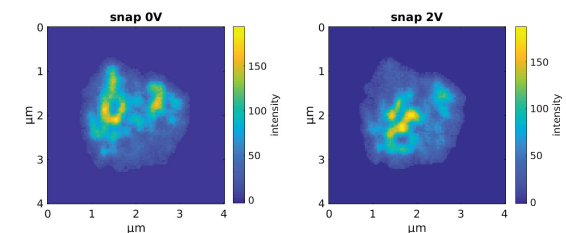


An objective lens composed of several beryllium lenses magnifies the projection of a diffracting grain.

Strain map



In another experiment run at 900 °C, snapshots at 0V and 2V were taken with an interval of few seconds. The internal processes of the electrolyte grains are unknown, further investigations are expected to provide more information.



References

- H. Simons, et al., Nature Communications. DOI: 10.1038/ncomms7098. 2015
- R. Knibbe, et al., Journal of The Electrochemical Society, 157 (8) B1209-B1217 2010
- F. Tietz, et al., Journal of Power Sources, 223 (2013) 129-135
- A. Hagen, et al., Journal of Synchrotron Radiation (2012), 19, 400-407. DOI: 10.1107/S0909049512006760

Acknowledgements

This project is in collaboration with the ESRF Beamline ID06.

We thank the ERC Advanced Grant



Elucidating the Orientation and Interactions of Modified Cellulose Nanocrystal Networks

Karin Sahlin^{1,5}, Lilian Forsgren², Tobias Moberg^{2,5}, Ann Terry⁴, Tomás Plivelic⁴, Mikael Rigdahl^{2,5}, Gunnar Westman^{1,5}

Background

A lot of research efforts are put into replacing fossil-based materials with bio-based materials in order to address some of the challenges our society is facing, such as global warming and achieving a sustainable bio-based economy. It is important that these new materials show at least the same, or better, performance and properties as the current materials on the market, and cellulose is considered an interesting substitute. Cellulose nanocrystals, CNCs, show promise as a reinforcement elements in polymeric composites, among other applications, due to their excellent mechanical properties. There is however an issue with compatibility between the hydrophilic cellulose and the often hydrophobic polymer matrix that prevents achieving the desired performance. This can be addressed by chemically modifying the CNCs with functionalities more prone to interact with the matrix. The compatibility is however not the only parameter affecting the performance, the orientation and interactions of the needle-like nanocrystals will also impact the properties and are therefore important to understand.

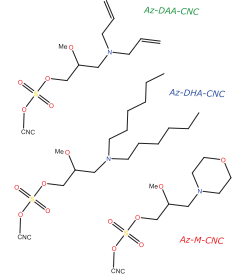
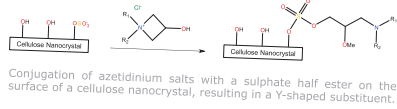
By understanding the molecular interactions and how these influences the orientation and network formation, modifications can more easily be tailored for desired properties and performance. The use of small angle X-ray scattering can enable the understanding of these systems by studying the molecular arrangement and structure.

Functionalisation of CNCs

The reaction presented here is the foundation of a completely new toolbox for tuning the performance and compatibility of cellulose nanocrystals, CNCs. By reacting CNCs with azetidinium salts, more CNCs with tailored properties can be achieved.

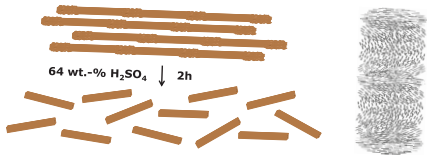
Three different functionalities have been investigated in this study, prepared from three different amines; diallyl amine, dihexyl amine and morpholine.

Through a combination of several characterisation techniques as well as model reactions, it has been shown that azetidinium salts can conjugate with sulphate half esters on the surface of CNCs.^[1] The azetidinium salts are reactive under mild conditions due to the inherent four-atom ring strain and the conjugation results in a Y-shaped substituent.



Cellulose Nanocrystals

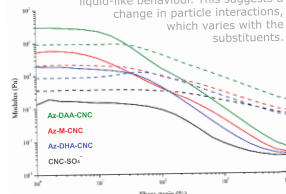
Cellulose nanocrystals, CNCs, are rod-like particles made up of highly ordered cellulose. They are prepared through acid hydrolysis of native cellulose, followed by removal of excess acid and sonication in order to achieve a colloidal stable suspension. The width of the CNCs is around 6 nm and the length is around 150-200 nm. As a result of the hydrolysis the surface is decorated with a small amount of sulphate half esters, which improve the colloidal stability. CNCs also forms chiral nematic phases, which has interesting optical properties and can also affect the mechanical properties the material.



Rheological Behaviour

The rheological behaviour of the unmodified as well as the modified CNCs was evaluated. Modification resulted in a significantly higher shear viscosity, with varying effect based on the functionalisation. The onset of percolation was shifted from 2.5 wt.-% for the unmodified to below 0.5 wt.-% for the modified CNCs.^[2]

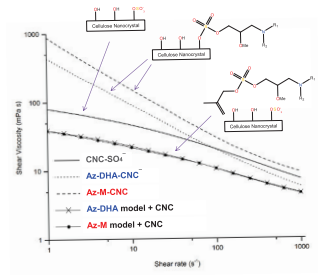
At 1.3 wt.-% all modified samples exhibit a gel-like behaviour, while the unmodified exhibits a liquid-like behaviour. This suggests a change in particle interactions, which varies with the substituents.



Storage (—) and loss (---) modulus for 1.3 wt.-% solutions of unmodified CNC, Az-M-CNC, Az-DHA-CNC and Az-DAA-CNC.

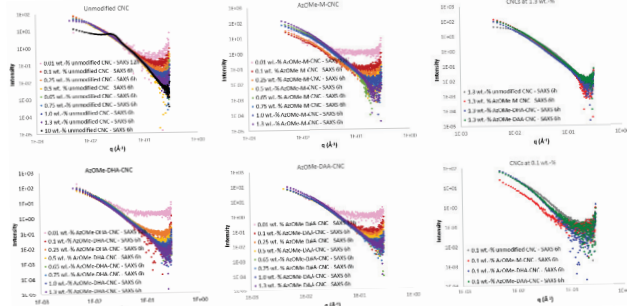
Upon modification, the CNCs show a significant increase in shear viscosity. The opposite is observed when a model substance was reacted with azetidinium salts and then mixed with unmodified CNCs.

At higher shear, there is a crossover of the storage and loss moduli for the modified CNCs. This indicates that the network is disrupted and the suspension will have a liquid-like behavior at high shear.



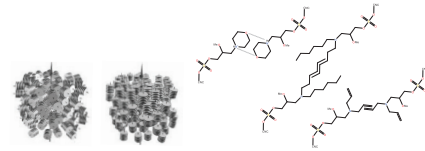
Small Angle X-ray Scattering

SAXS measurements were carried out on a SAXSLAB Mat: Nordic lab instrument with a Rigaku 003+ X-ray Microfocus Cu-radiation source and a Pilatus 300K detector. The measurements were performed at several concentrations, in order to detect any change in network formation. The graphs presented to the right are normalised to sample concentration to visualise concentration dependence.



Proposed Interactions

More work has to be carried out before any conclusions can be made regarding the structures of the networks, but a possible explanation for the differences may be due to the nature of the substituent interactions. The morpholine functionality is prone to hydrogen bonding, while the dihexyl substituents are hydrophobic and are therefore likely to have hydrophobic interactions and the diallyl functionalities could interact by π - π -stacking. This may influence the way they orient and what phases they form.



Affiliation

- ¹ Department of Chemistry and Chemical Engineering, Chalmers University of Technology, Gothenburg, Sweden
² Department of Industrial and Materials Science, Chalmers University of Technology, Gothenburg, Sweden
³ Swedish NMR Centre, University of Gothenburg, Gothenburg, Sweden
⁴ MAX IV Laboratory, Lund University, Lund, Sweden
⁵ Wallenberg Wood Science Center, Chalmers University of Technology, Gothenburg, Sweden

Contact information

Telephone: +46 31 772 3065
E-mail: karin.sahlin@chalmers.se



WWSC is a joint research center at KTH and Chalmers

References

- [1] Börjesson, M.; Sahlin, K.; Bernin, D.; Westman, G., Increased thermal stability of nanocellulose composites by functionalization of the sulfate groups on cellulose nanocrystals with azetidinium ions, J. Appl. Polym. Sci. 2017, 135, 45963
[2] Sahlin, K.; Forsgren, L.; Moberg, T.; Bernin, D.; Rigdahl, M.; Westman, G., Surface treatment of cellulose nanocrystals (CNC) - effects on dispersion rheology, Cellulose 2017



Towards SANS studies of a repressor-antirepressor complex from a phage genetic switch

Kim Krighaar Rasmussen¹, Andres Palencia², Malene Ringkjøbing Jensen³, S. Zöe Fisher⁴, Leila Lo Leggio¹

¹Biological Chemistry, Department of Chemistry, University of Copenhagen. ²Institute for Advanced Biosciences, INSERM U1209, CNRS UMR85309, Université Grenoble Alpes, Grenoble, France. ³Université Grenoble Alpes, CNRS, CEA, Institut de Biologie Structurale, Grenoble, France. ⁴Department of Biology, Lund University, 35 Sölvegatan, 22362, Lund, Sweden.

Introduction

Bacteriophages are bacteria virus particles, which can be classified as lytic or temperate depending on the fate infected cells will face. Lytic bacteriophages instigate synthesis of new progeny directly after infection, whereas temperate bacteriophages have the ability to either be lytic or lysogenic. In the lysogenic life cycle the bacteriophage will stay latent in the bacterium's genome until an external factor signals it to switch to the lytic life cycle, and hence production of progeny.

TP901-1 is an example of a temperate bacteriophage infecting *Lactococcus lactis*, a bacterial strain heavily used in the dairy industry. After infection, TP901-1 uses the host transcription machinery to transcribe *cl* and *mor* coding for the two main regulatory proteins of the genetic switch². CI forms a hexamer, and binds to three palindromic operator sites O_R , O_L and O_D , which represses the lytic life cycle promoter (P_L). The other protein MOR has been suggested to bind to CI, forming a complex, which binds to a still unknown DNA sequence in order to repress the lysogenic life cycle promoter² (P_R) (Fig 1 A). Until now no structural studies have been performed on MOR. For CI structural studies have shown that CI consists of a helix turn helix (HTH) domain responsible for DNA binding, a flexible linker providing CI with the necessary flexibility for optimal DNA binding^{3,4}. The C-terminal domain of CI (CTD) is responsible for oligomerization of the hexamer. A part of CTD, CTD1, is responsible for the dimerization. A truncated variant of CI, CI Δ 58, that contains NTD, linker and CTD1, has previously been shown to constitute the binding unit for the O_L site⁴.

Here we present our progress in producing, characterizing and purifying stable binary (protein/DNA) and ternary (protein, deuterated protein and DNA) complexes, to be used in future small angle neutron scattering contrast variation studies.

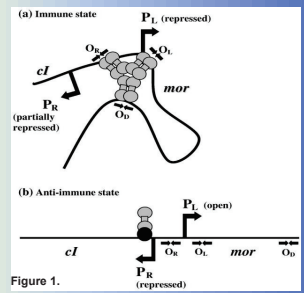


Figure 1.

Overview of the system

Deuterated proteins

Binding partners

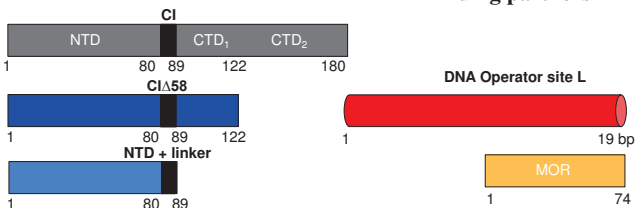


Figure 2. Overview of proteins (grey, dark blue, light blue, yellow) and DNA (red) used until now.

Purification of complexes

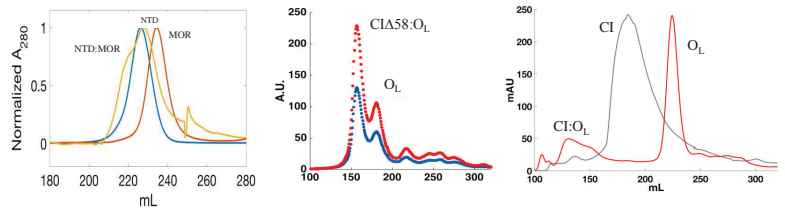


Figure 3. Purification of complexes with size exclusion chromatography

K_d of CI:MOR interaction

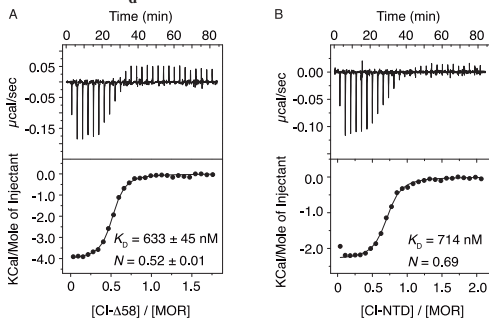


Figure 4. Determination of K_d with Isothermal Calorimetric. A) CI Δ 58:MOR, B) CI-NTD:MOR

Characterization of complex samples

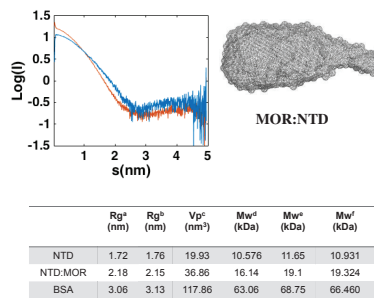
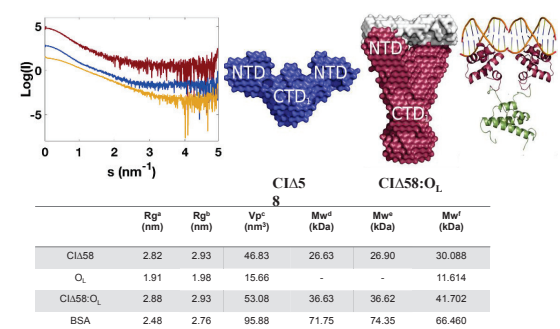


Figure 5. SAXS studies of complexes (NTD:MOR, CI Δ 58:O_L)

Initial scattering analysis with SAXS



Simulated I(0) in contrast variation experiment of complexes

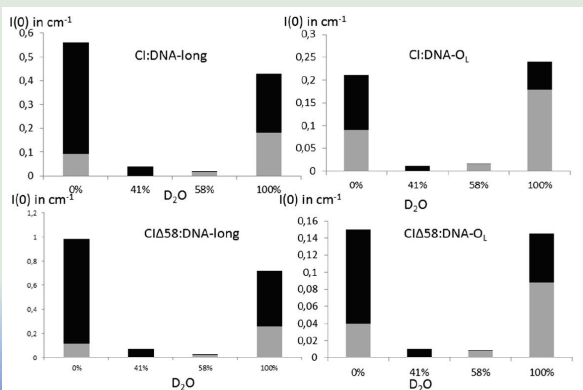


Figure 6. DNA contribution in black, protein in grey

Results and Discussion

To investigate the protein:protein and protein:DNA arrangement in the two life cycle of the genetic switch based in bacteriophage TP901-1, we aim to carry out small angle Neutron scattering contrast variation experiments. We here show that it is possible to co-purify NTD:MOR, CI Δ 58:O_L and CI:O_L, a necessary step to obtain monodisperse samples. We also show that the affinity between NTD:MOR, CI Δ 58:MOR is suitable for preparing stable heteromer complex. This was also evident from initial SAXS studies, but more important the SAXS studies strongly indicates SANS studies should be possible. Although, the simulated I(0) indicates, that we need to increase the concentrations compared to SAXS studies, as these were calculated with 3 mg/mL and 1.5 mg/mL. Three CI variant (CI, CI Δ 58 and NTD) has been deuterated, and are ready to be purified for further investigation with neutrons.

Acknowledgement

We like to thank the beam scientist at BM29, ESRF Dr. Martha Brennich for helpful discussions, and providing beam time.

Reference

- Gardner, T. S., Cantor, C. R. & Collins, J. J. Construction of a genetic toggle switch in *Escherichia coli*. *Nature* **403**, 339–342 (2000).
- Pedersen, M. & Hammer, K. The role of MOR and the CI operator sites on the genetic switch of the temperate bacteriophage TP901-1. *J. Mol. Biol.* **384**, 577–589 (2008).
- Frandsen, K. H. et al. Binding of the N-terminal domain of the lactococcal bacteriophage TP901-1 CI repressor to its target DNA: a crystallography, small angle scattering and NMR study. *Biochemistry* **13092093647008** (2013). doi:10.1021/bi400439y
- Rasmussen, K. K. et al. Structural and dynamics studies of a truncated variant of CI repressor from bacteriophage TP901-1. *Scientific Reports* **6**, 29574 (2016).

A surface active enzyme and colonization factor investigated by x-ray and neutron scattering

Henrik V. Sørensen¹, Kathryn L. Browning², Reidar Lund¹, Ute Krenzel¹, Kaare Bjerregaard-Andersen¹

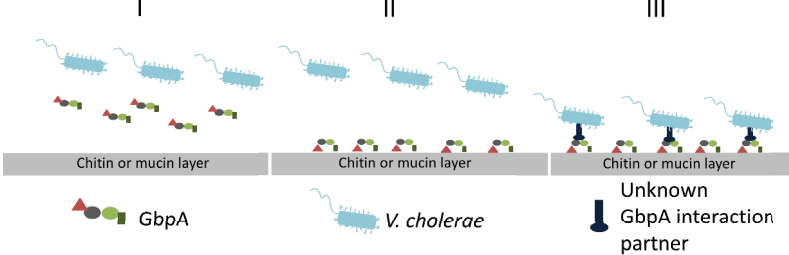
¹ Department of Chemistry, University of Oslo, Sem Sælands vei 26, 0371, Oslo, Norway

² Department of Pharmacy, University of Copenhagen, Universitetsparken 2, 2100 København Ø, Denmark

Aim

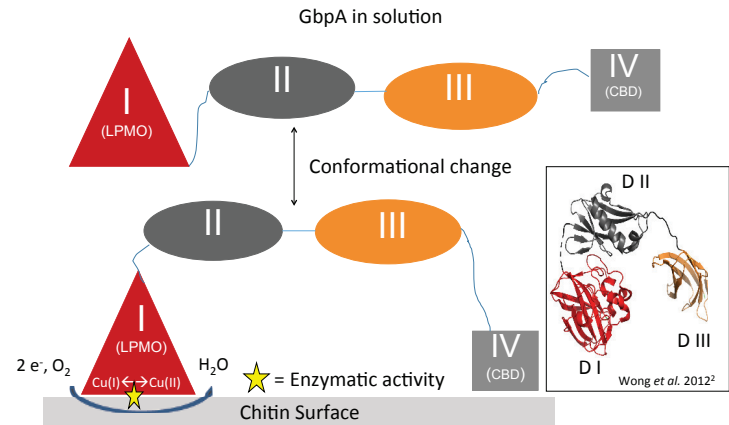
Elucidate the solution and surface bound conformational states of *V. cholerae* colonization factor *N*-acetyl glucosamine binding protein A (GbpA).

The mechanism of colonization by *Vibrio cholerae*



V. cholerae secretes GbpA, which mediates the attachment of the bacterium to chitin or intestinal mucin.

GbpA binds and degrades chitin surfaces



Approach

We want to combine high resolution diffraction data with SAXS/SANS to get insight into the solution structure of GbpA. By furthermore using neutron reflectometry, we can potentially map the conformational state of GbpA on the surface of chitin.

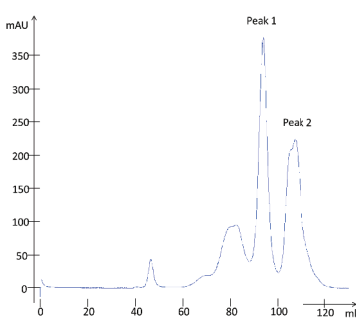
To do this, we need:

1. Expressed and purified GbpA – monodisperse and >95 % pure.
2. Perdeuterated GbpA – may be needed for SANS.
3. Smooth chitin surfaces – surface roughness <10 Å.

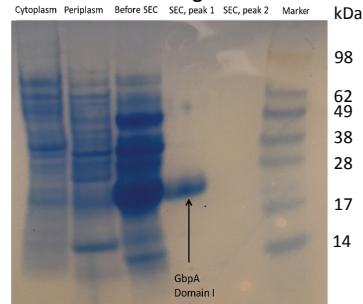
Protein purification

Production of GbpA and individual domains of GbpA for structural studies is done by expression in *Escherichia coli* cells. GbpA is then isolated from periplasm and purified by anion-exchange chromatography followed by size-exclusion chromatography.

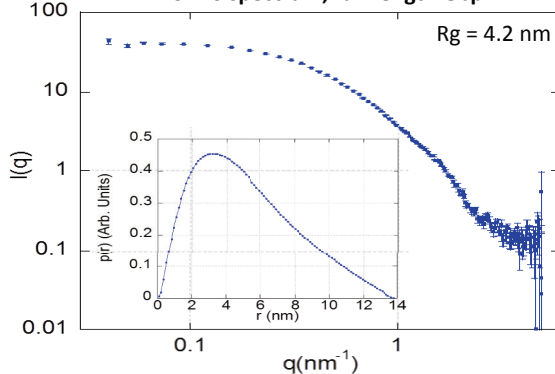
Size-exclusion chromatography (SEC)



SDS-Page

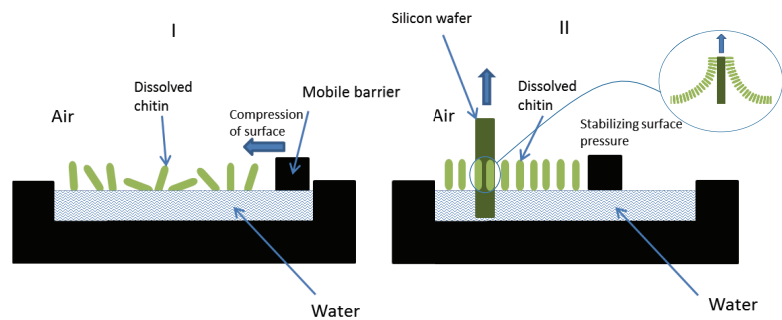


SAXS spectrum, full-length GbpA

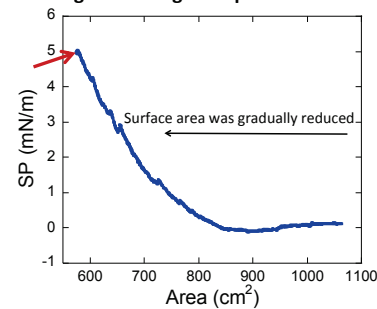


Saxs spectrum of full-length GbpA at 37°C. A radius of gyration of 4.2 nm corresponds to an elongated molecule based on the dimensions obtained from the crystal structure. The shape of the pair-distance distribution function also indicates an elongated protein.

Langmuir-Blodgett deposition of chitin on silicon

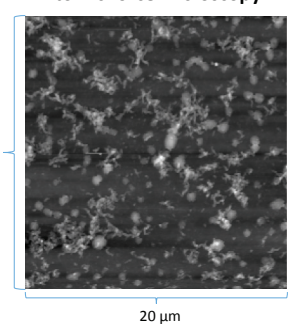


Langmuir-Blodgett deposition of chitin



At surface pressure 5 mN/m (red arrow), the pressure was stabilized and chitin was deposited on silicon wafer. Protocol modified from Taira *et al.* 2014⁴.

Atomic force microscopy



Atomic force microscopy reveals that the chitin was successfully deposited on the surface of silicon. The surface is covered by a layer of chitin, but also with aggregates on top.

Challenges

While a robust purification protocol that allows large scale production of GbpA has been established, several challenges are still present:

1. Generation of highly smooth chitin layers that interact with GbpA and can be studied by neutron reflectometry.
2. Development of a perdeuteration protocol. This requires optimization of protein expression in enhanced minimal media.

Key references: ¹ Kirn *et al.*, *Nature*, 2004, 438, 863-866, ² Wong *et al.*, *Plos Pathogens*, 2012, 8 (1): e1002373, ³ Loose, J.S. *et al.*, *FEBS Lett.*, 2014, 588(18): 3435-40, ⁴ Taira, Y. and C.E. McNamee. *Soft Matter*, 2014, 10(42): p. 8558-72.

Linking brain tissue capturing modalities: ultra-high resolution synchrotron imaging and low resolution MRI

Mariam Andersson^{1,2}, Vedrana Andersen Dahl², Hans Martin Kjer^{1,2}, Martin Bech³, Alexandra Pacureanu⁴, Anders Bjorholm Dahl², Tim B. Dyrby^{1,2}.

¹ Danish Research Centre for Magnetic Resonance, Copenhagen University Hospital Hvidovre, Hvidovre, Denmark

² Department of Applied Mathematics and Computer Science, Technical University of Denmark, Kongens Lyngby, Denmark

³ Department of Medical Radiation Physics, Clinical Sciences, Lund University, Lund, Sweden

⁴ European Synchrotron Radiation Facility, Grenoble, France

Abstract

Tissue from the different white matter regions of a monkey brain was prepared and imaged by phase contrast tomography at the synchrotrons DESY and ESRF. An initial segmentation of the volumetric images reveals the relative trajectories of blood vessels and axons, axonal twisting and a complex microstructural environment never before described.

The acquired anatomical information can contribute to the improvement of existing biophysical MRI models such that they reflect the true microstructural anatomy in the brain.

Initial Segmentation

The volumetric synchrotron images were downsampled and filtered to make operations on them less computationally intensive. Blood vessels could be segmented by thresholding the lighter areas of the image and manually initialising region growing snakes in ITK-Snap. For the axon segmentation, a manual segmentation of a single slice was performed and used to train a myelin classifier. The posterior probability of the myelin obtained from the classifier was thresholded and combined with region growing snakes to segment the interiors of the axons. Initial segmentations are shown in Figures 2-5.

Background

Neurodegenerative diseases, such as Alzheimer's, cause anatomical changes to axons and their surrounding myelin sheaths. Non-invasive MRI methods can estimate these changes, but are limited to resolutions on the order of mm and the biophysical models [1,2] on which they are based make incorrect assumptions about 3D axon morphology which skew the results i.e. they assume that axons are straight. X-ray phase contrast tomography enables high-resolution 3D imaging of the microstructural tissue environment, required to improve the biophysical axon model and realise advances in in-vivo histology with clinical MRI.

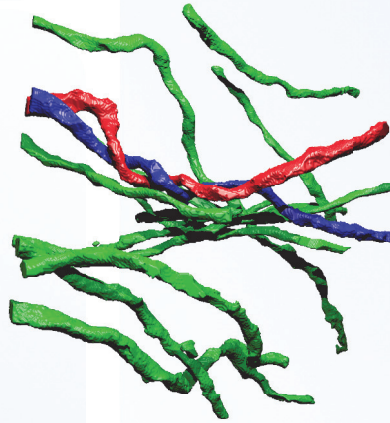


Figure 5. Crossing fibre region of the monkey brain, ESRF data. Axonal twisting displayed in two axons shown in red and blue. Surrounding axons are shown in green.

Figure 2. Data obtained from ID16A, ESRF, showing a slice through a crossing fibre region of the monkey brain. Axons are shown in yellow and blood vessels in red.

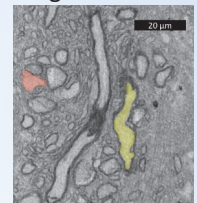


Figure 3. Crossing fibre region of the monkey brain, ESRF data. Axons (yellow) and vessels (red).

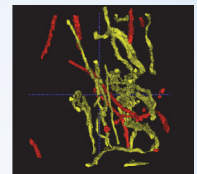
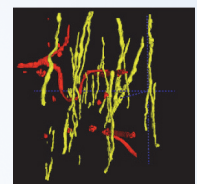


Figure 4. Mid-body corpus callosum of the monkey brain, ESRF data. Axons (yellow) and vessels (red).



X-ray Phase Contrast Tomography

Tissue biopsies from the white matter of an Old World Vervet monkey were extracted as shown in Figure 1, stained with Osmium (to give contrast to the fatty myelin sheaths around the axons), embedded in EPON or paraffin and imaged at beamline P10 of PETRA III (DESY) and ID16A of ESRF at varying resolutions and fields of view.



Figure 1. Sagittal slice of monkey brain showing various locations from which biopsies were taken.

Perspective

Phase contrast tomography at synchrotrons has provided access to unique, 3D information with regards to the microstructural environment in the brain. Further studies could involve the use of a disease model to compare microstructural characteristics between healthy and diseased tissues.

References

- [1] S. N. Jespersen, H. Lundell, C. K. Søndersby, and T. B. Dyrby, "Commentary on 'Microanisotropy imaging: quantification of microscopic diffusion anisotropy and orientation of order parameter by diffusion MRI with magic-angle spinning of the q-vector'" *Frontiers in Physics*, vol. 2, p. 28, 2014.
- [2] H. Lundell, C. K. Søndersby, and T. B. Dyrby, "Diffusion weighted imaging with circularly polarized oscillating gradients," *Magn. Reson. Med.*, vol. 73, no. 3, pp. 1171–1176, 2015.

Funding

This project is funded by the Capital Region Research Foundation (grant number: A5657)

Geometrical Characterisation of UD Composites through X-ray micro-CT and Individual Fibre Tracking



Monica J. Emerson (monj@dtu.dk), Kristine M. Jespersen, Lars P. Mikkelsen, Philip J. Withers, Ying Wang, Knut Conradsen, Vedrana A. Dahl, Anders B. Dahl

MOTIVATION

Wind turbines with longer blades produce **more power** and will decrease the **cost of energy**.

To build longer blades we need composites that are:

- Stronger
- Stiffer
- More resistant to fatigue

TASK

The **load bearing parts*** of the blades are made of UD composites.

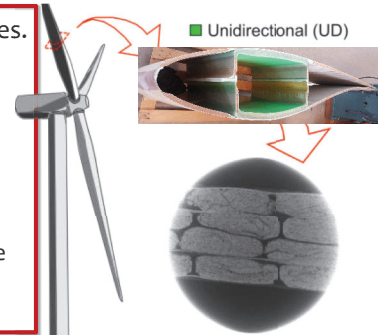
By **combining**: X-ray micro-CT, ultra-fast imaging and individual fibre tracking

We can **measure**: Fibre geometry and its changes under load with **high precision**

To **understand**:

The link between the manufacturing processes, the real micro-structure and the mechanical properties of real composites.

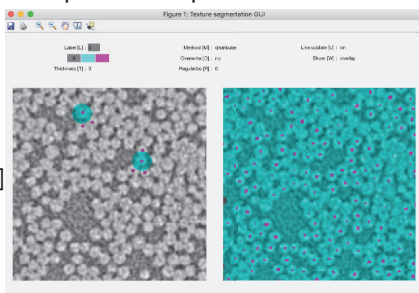
* green parts in the blade on the right



Dictionary-based segmentation:

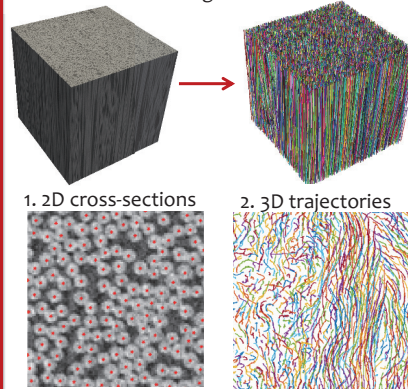
1. Flexible segmentation of material structures
2. User-friendly training with immediate feedback
3. Minimal user input and adaptable to the data-set

Detecting fibre cross-sections with our GUI [3]



Fibre Geometry Determination

via Individual Fibre Segmentation



The data we support:

1. Densely packed UD fibres
2. A range of fibre and matrix materials
3. Fields of view (FoV) of a representative size
4. Relatively low quality scans to enable:
 - a) Reasonably fast scans at lab sources
 - b) Time-lapse in-situ loading experiments
 - c) Fast scanning and analysis of large FoV

Challenges in this data:

- Limited contrast between material phases
- Noise and artefacts from CT imaging
- Reduced spatial resolution (blurriness, pixellation...)

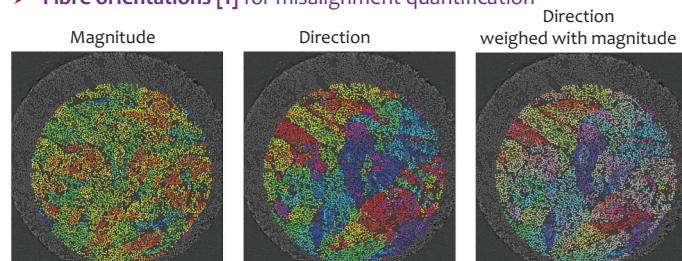
Scan to download article
Individual fibre segmentation [1]



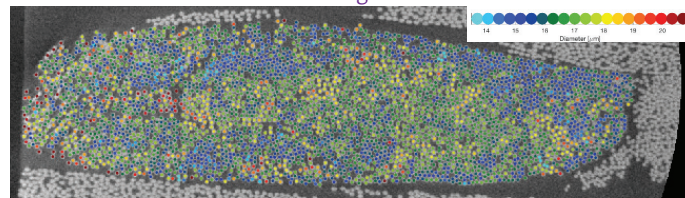
APPLICATIONS:

1. Characterisation of Real Structures

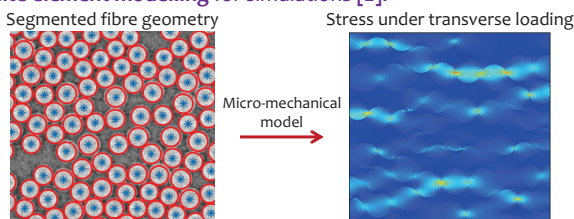
➤ **Fibre orientations** [1] for misalignment quantification



➤ **Fibre diameters** [4] for e.g. investigating the effects and randomness in fibre manufacturing



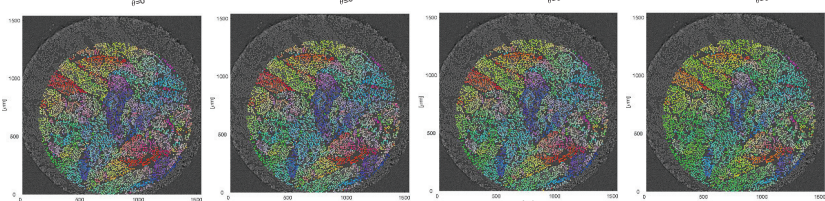
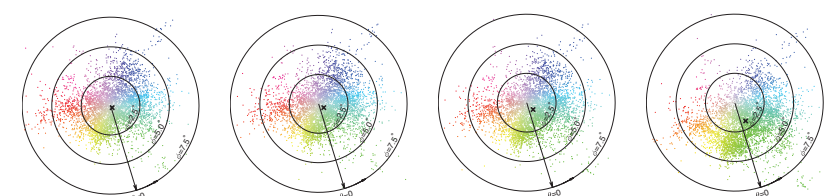
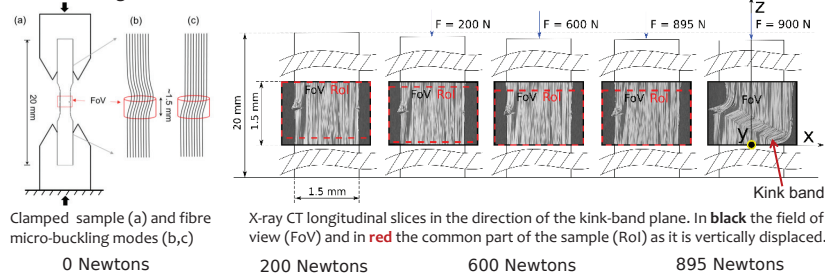
➤ **Finite element modelling** for simulations [2].



2. Evolution of Structures under Load

Ultra-fast imaging while compressing a composite in-situ

AIM: Investigate fibre micro-buckling and kink-band formation by tracking individual fibres [5]



SOME OF THE FINDINGS IN [5]

- At 25% of the failure load, fibres have started to tilt in approximately the kink direction
- Initially, there is a lack of fibres in the direction opposite to the kink

References

- [1] Emerson MJ, Jespersen KM, Dahl AB, Conradsen K and Mikkelsen LP. Individual fibre segmentation from 3D X-ray computed tomography for characterising the fibre orientation in unidirectional composite materials. *Composites Part A: Applied Science and Manufacturing* 2017.
- [2] Mikkelsen LP, Emerson MJ, Jespersen KM, Dahl VA, Conradsen K and Dahl AB. X-ray based micromechanical finite element modeling of composite materials. In *Proceedings of 29th Nordic Seminar on Computational Mechanics* 2016.
- [3] Dahl, V. A., Trinderup, C. H., Emerson, M. J. and Dahl, A. B. Content-based propagation of user markings for interactive segmentation of patterned images. To be submitted in March 2018 to *IEEE Transactions on Image Processing*.
- [4] Emerson, M. J., Dahl, V. A., Conradsen, K., Dahl A. B. and Mikkelsen L. P. Statistical validation of individual fibre segmentation from tomograms and microscopy. *Composites Science and Technology* 2018, accepted subject to minor revision.
- [5] Emerson, M. J., Wang, Y., Dahl, A. B., Withers, P. J., Conradsen, K. and Dahl, V. A. Quantifying fibre reorientation during axial compression of a composite through time-lapse X-ray imaging and fibre tracking. *Submitted to Composites Science and Technology* 2018.

Dynamics of Microscale Precursors Establish Brittle-Compressive Failure in Rocks as a Critical Phenomena

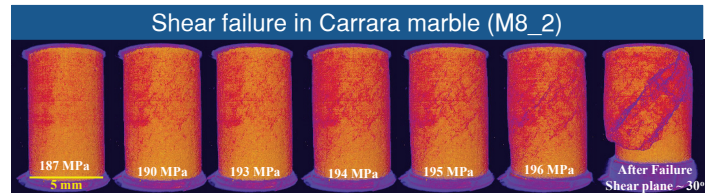
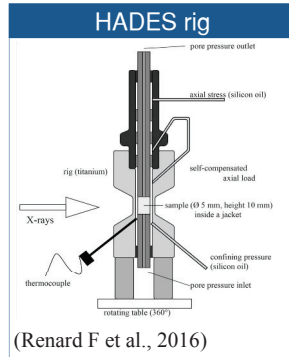
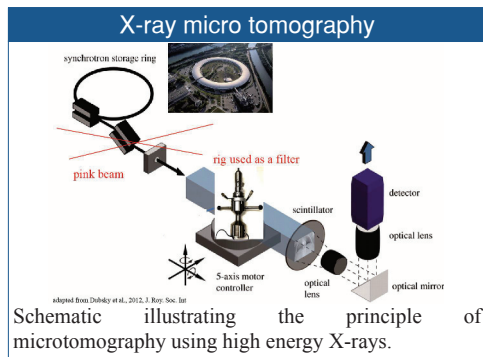
Neelima Kandula*¹, Francois Renard^{1,3}, Jerome Weiss², Dag Kristian Dysthe¹, Benoit Cordonnier^{1,3} and Maya Kobchenko¹

1. Departments of Physics and Geosciences, PGP, University of Oslo, P O Box 1048, Blindern, Oslo 0316, Norway
 2. ISTERre, University Grenoble, Alpes and CNRS, CS40700, Grenoble 38058, France
 3. The European Synchrotron, ESRF, beamline ID19, Grenoble, France
- *neelima.kandula@geo.uio.no

1. Introduction

- Earlier studies on deformation of rocks have indicated the existence of precursory signals before failure (Lockner et al., 1991) and final rupture is a critical point (Girard et al., 2010). We present a quantitative analysis of physical mechanisms governing the nucleation and growth of fracture at microscale that is giving rise to macroscopic failure in crustal rocks.
- We have used a novel experimental technique that couples X-ray microtomography with a unique triaxial deformation apparatus, HADES, that can provide 3D-time series images of microstructural evolution towards failure at micrometer resolution.
- These data allow characterizing the spatial and time correlations (power law) that govern the initiation of damage and the development of precursors to macroscopic failure.

2. Experimental methods



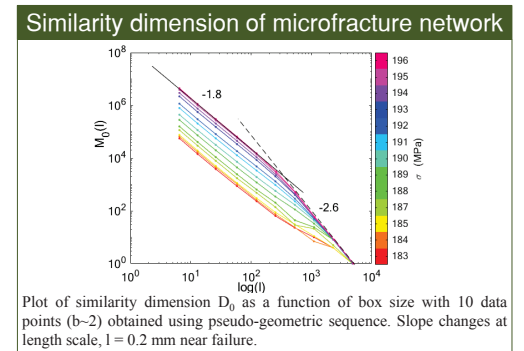
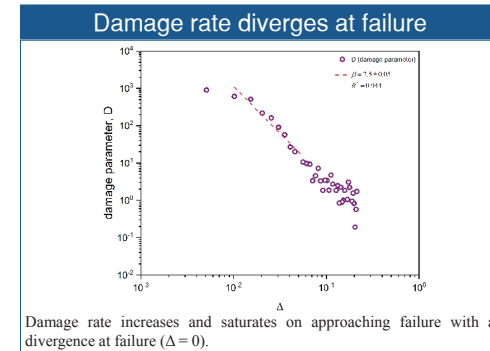
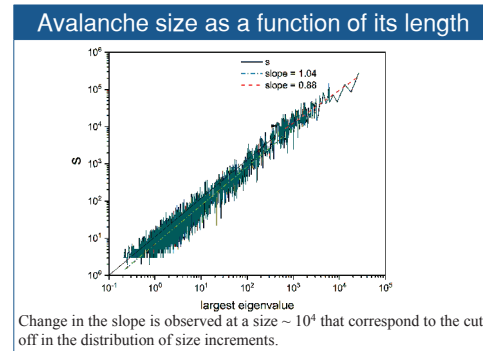
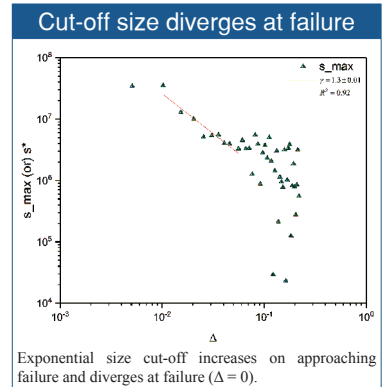
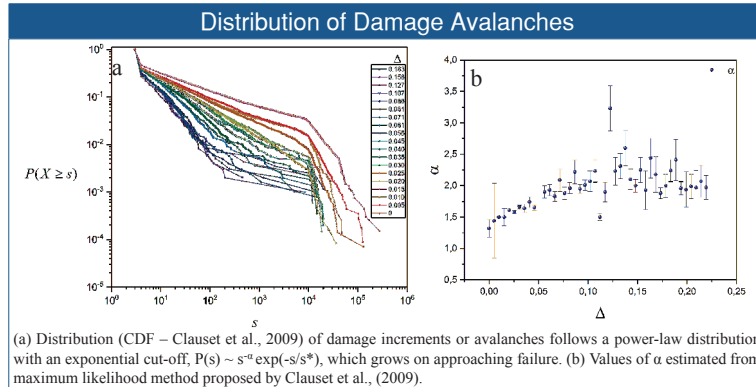
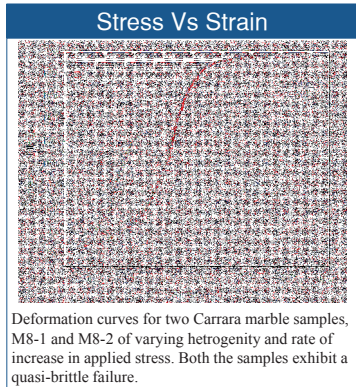
Experimental Conditions			
Sample	Confining Pressure (MPa)	Failure Point (MPa)	Pore Pressure (MPa)
M8-1	20	130	0
M8-2	25	196/197	0
M8-3	30	199	0
M8-4	23	200	10

- This technique provides access to the microstructure of the sample during deformation at a spatial resolution of 6.5µm and at lab time scale.
- 2D cross-sections for each scan are reconstructed into a 3D volume.

3. Results

Index for parameters in the analysis

$s(\sigma)$ or s – microfracture size increments or avalanches; S_{max} = size of the largest cluster; s^* = upper cut-off size in the distribution; ϕ = volume of microfractures or porosity of the sample; ϕ_i = initial porosity; σ = applied axial stress; σ_f = stress at failure; $D = (\phi - \phi_i) / \phi_i$: damage index; $\Delta = (\sigma_f - \sigma) / \sigma$: control parameter, measure of distance from failure;



4. Conclusion

- Scaling laws and fractal dimensions obtained for the present system of a non-porous rock that exhibit a quasi-brittle mechanical behavior argue that failure in this case is a critical phenomenon using Progressive Damage Model (Girard et al., 2010)
- Saturation of damage rate and size cut-off in distribution of damage increments hints for presence of mechanisms like sub-critical crack growth and percolation.
- Time resolved X-ray micro tomography coupled with triaxial deformation apparatus is an adaptable tool for understanding the physical laws governing the route to shear failure.

5. References

- Lockner, D., Byerlee, J. D., Kuksenko, V., Ponomarev, A., & Sidorin, A. (1991). Quasi-static fault growth and shear fracture energy in granite. *Nature*, 350(6313), 39-42.
- Girard, L., Amitrano, D., & Weiss, J. (2010). Failure as a critical phenomenon in a progressive damage model. *Journal of Statistical Mechanics: Theory and Experiment*, 2010(01), P01013.
- Renard, F., Cordonnier, B., Dysthe, D. K., Boller, E., Tafforeau, P., & Rack, A. (2016). A deformation rig for synchrotron microtomography studies of geomaterials under conditions down to 10 km depth in the Earth. *Journal of Synchrotron Radiation*, 23(4).
- Clauset, A., Shalizi, C. R., & Newman, M. E. (2009). Power-law distributions in empirical data. *SIAM review*, 51(4), 661-703.

Computed Tomography using a Weighted Shearlet-based Sparsity Penalty

N A B Riis¹ (nabr@dtu.dk), J Frøsig², Y Dong¹, and P C Hansen¹

¹ DTU Compute, Richard Petersens Plads, Building 324, DK-2800 Kgs. Lyngby, Denmark

² FORCE Technology, Park Alle 345, DK-2605 Brøndby, Denmark

Introduction: Case study [1]

Task: Inspection of underwater oil pipes for defects, cracks and residue buildup.

Problem: A narrow and high intensity X-Ray beam is needed to penetrate the steel pipe.
→ Unable to illuminate the entire pipe.
→ Potential artifacts in reconstruction.

Goal: Develop new scanning and reconstruction methodology that allows to:

- Capture details of entire pipe.
- Avoid limited-data artifacts.
- Use as few measurements as possible.

Scanning method

Microlocal analysis [2] provides a way to determine which material layers are captured in a full rotation for a given type of scan.

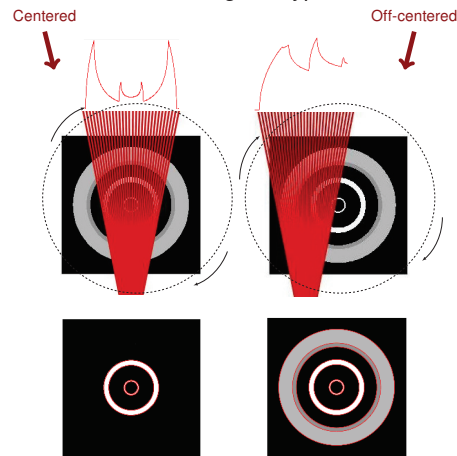


Figure 1: Illustration of the captured material layers for two scanning methods.

According to the theory, an off-centered beam captures more material layers and possible defects of the pipe.

Results

Scanning off-center and using a shearlet-based reconstruction method improves image quality by avoiding limited-data artifacts:

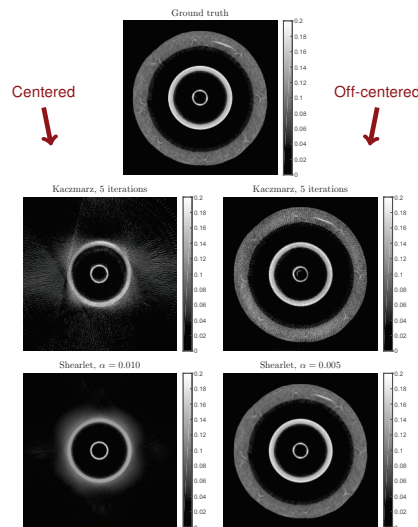


Figure 2: Reconstructions from real pipe data with 180 measurements. Kaczmarz algorithm [3] is with non-negativity.

The shearlet method maintains reconstruction quality with fewer measurements:

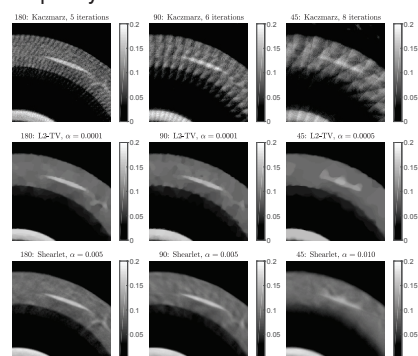


Figure 3: Reconstructions for a reduced number of measurements (180, 90, 45).

Reconstruction method

Discrete model of the scanning process:

$$\mathbf{A}\mathbf{x} \approx \mathbf{b}, \quad (1)$$

$\mathbf{A} \in \mathbb{R}^{m \times n}$ is the discretized Radon transform, $\mathbf{x} \in \mathbb{R}^n$ represents reconstruction ← **unknown**, $\mathbf{b} \in \mathbb{R}^m$ are the noisy measurements.

Reconstruction based on a sparse representation of the image by **shearlets**:

$$\min_{\mathbf{x} \geq 0} \frac{1}{2} \|\mathbf{A}\mathbf{x} - \mathbf{b}\|_2^2 + \alpha \|\mathbf{W}\Phi\mathbf{x}\|_1, \quad (2)$$

$\alpha > 0$ is the regularization parameter, $\mathbf{W} = \text{diag}(w_i) \in \mathbb{R}^{p \times p}$ with weights $w_i \geq 0$, $\Phi \in \mathbb{R}^{p \times n}$ is the shearlet analysis transform.

Shearlets are optimally sparse for representing discontinuities along curved edges in images [4] → high level of regularization without removing details.

We solve (2) using the ADMM method [5]. Auxiliary variable $\mathbf{c} = \Phi\mathbf{x}$. Iterative updates:

$$\mathbf{x}^{k+1} := \min_{\mathbf{x} \geq 0} \frac{1}{2} \|\mathbf{A}\mathbf{x} - \mathbf{b}\|_2^2 + \frac{\rho}{2} \|\Phi\mathbf{x} - \mathbf{c}^k + \mathbf{u}^k\|_2^2, \quad (3)$$

$$\mathbf{c}^{k+1} := \min_{\mathbf{c}} \alpha \|\mathbf{W}\mathbf{c}\|_1 + \frac{\rho}{2} \|\Phi\mathbf{x}^{k+1} - \mathbf{c} + \mathbf{u}^k\|_2^2, \quad (4)$$

$$\mathbf{u}^{k+1} := \mathbf{u}^k + \Phi\mathbf{x}^{k+1} - \mathbf{c}^{k+1}, \quad (5)$$

\mathbf{u} are scaled Lagrange multipliers and $\rho > 0$.

The updates are calculated using:

(3): CGLS [6] + non-negativity projection.

(4): Element-wise soft thresholding.

Conclusion

With limited measurements and a narrow beam a **shearlet-based reconstruction** provide greatly improved CT images compared to standard methods as shown by the case study on real oil pipe data measured with an **off-centered scan**.

References

- [1] N. A. B. Riis, J. Frøsig, Y. Dong, and P. C. Hansen. Limited-data X-Ray CT for underwater pipeline inspection. *Inverse Problems*, 34(3):034002, 2018.
- [2] Venkateswaran P. Krishnan and Eric Todd Quinto. Microlocal analysis in tomography. In Otmar Scherzer, editor, *Handbook of Mathematical Methods in Imaging*, pages 847–902. Springer-Verlag New York, 2 edition, 2015.
- [3] Gabor T. Herman. *Fundamentals of Computerized Tomography: Image Reconstruction from Projections*. Springer, 2 edition, 2009.
- [4] Gitta Kutyniok and Wang-Q Lim. Compactly supported shearlets are optimally sparse. *Journal of Approximation Theory*, 163(11):1564–1589, 2011.
- [5] Stephen Boyd, Neal Parikh, Eric Chu, Borja Peleato, and Jonathan Eckstein. Distributed optimization and statistical learning via the alternating direction method of multipliers. *Foundations and Trends in Machine Learning*, 3(1):1–122, 2010.
- [6] Åke Björck. *Numerical Methods for Least Squares Problems*. SIAM, 1996.

Acknowledgements

We thank FORCE Technology for their collaboration on this project and for providing data. This work is a part of the HD-Tomo project funded by Advanced Grant No. 291405 from the European Research Council. The authors also acknowledge the financial support from CINEMA: the alliance for IMAGING of Energy Materials, DSF-grant no. 1305-00032B under the Danish Council for Strategic Research and from Interreg (MAX4ESSFUN).

Structural characterization of a Glucuronoyl Esterase from *Opiritus terrae*

*Rasmus Meland Knudsen*¹, *Scott Mazurkewich*^{2,3}, *Jens-Christian Navarro Poulsen*¹, *Jenny Arnlind Bååth*^{2,3}, *Lisbeth Olsson*^{2,3}, *Johan Larsbrink*^{2,3} and *Leila Lo Leggio*¹ *

* Leila@chem.ku.dk

1. University of Copenhagen, Dept. of Chemistry, Universitetsparken 5, DK-2100 KBH Ø, Denmark
2. Chalmers University of Technology, Division of Industrial Biotechnology, Dept. of Biology and Biological Engineering, Kemigården 1, SE-412 96 Gothenburg, Sweden
3. Chalmers University of Technology, Wallenberg Wood Science Center, Kemigården 1, SE-412 96 Gothenburg, Sweden

Background

Improvements in biomass conversion are needed to advance renewable resources technologies to ultimately achieve a petroleum free society. Lignocellulosic biomass consists mostly of cellulose, hemicellulose and lignin. Cellulose and hemicellulose are polysaccharides that, potentially, can be fermented into biofuels or converted to other high value products. The complete hydrolysis of plant matrix require the concerted action of many enzymes as the matrix is comprised by many carbohydrate and non-carbohydrate components linked by glycosidic-, ether- or ester-bonds. Glucuronoyl esterases (GEs), microbial enzymes discovered in 2006, break an ester bond between 4-O-Me-D-Glucuronic acids of glucuronoxylan and alcohols of lignin. These enzymes could have uses in biomass processing technologies, by helping remove the lignin from polysaccharides, making the biomass less recalcitrant [1]. GEs are classified into the Carbohydrate Esterase family 15 (CE15) of the Carbohydrate Active Enzymes database (<http://www.cazy.org>). Although potentially being important for bioprocessing, to-date very few of these enzymes have been biochemically characterized and only 2 protein structures of fungal origin [2][3] and 1 from bacterium origin [4] have been determined. Genome analysis of *Opiritus terrae*, a biomass fermenting soil bacterium originally isolated from rice paddy soil, shows that it has 4 different CE15 gene copies within its genome. These 4 CE15 genes (A through D) have been cloned, recombinantly produced and biochemically characterized as GEs. Here we focus on the structure determination of OtCE15A.

Crystallization and structure determination of OtCE15A

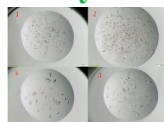


Figure 1:
2D optimization screen of the 4 best conditions.
1)B12: 0.1M Buffer system 3, 50% v/v Precipitant mix 4, 0.09M Halogens.
2)A4 : 0.1M buffer system 1, Precipitant mix 4, 0.06 Divalents.
3)C12: 0.1M buffer system 3, Precipitant mix 4, 0.09M NPS.
4)G12: 0.1M buffer system 3, Precipitant mix 4, 0.1M Carboxylic acids.

Buffer system 1: (imidazole, MES monohydrate (acid), pH 6.5 @ 20 °C) Buffer system 2: (Tris (base), BICINE, pH 8.5) Precipitant mix 4: (25% v/v MPD, 25% PEG 1000, 25% v/v PEG 3350) Ligands: (0.3M Sodium fluoride, 0.3M Sodium bromide, 0.3M Sodium iodide) Quaternary: (0.3M Magnesium chloride hexahydrate, 0.2M Calcium chloride dihydrate) D2S: (0.3M Sodium nitrate, 0.3 Sodium phosphate dibasic, 0.3M Ammonium sulfate) Carboxylic acids: (0.2M Sodium formate, 0.2M Ammonium acetate, 0.2M Sodium citrate tribasic dihydrate, 0.2M Sodium potassium tartrate tetrahydrate, 0.2M Sodium oxalate)

- Initial screening of OtCE15A with the Morpheus screen was performed in a stock protein concentration of 45 mg/ml in 20 mM TRIS pH 8.0 buffer.
- 2D optimization using the 4 best conditions, varying precipitant mix and protein concentration, was performed.
- Derivatization was carried out by adding 1.0 μL of crystallization mother liquor, followed by 0.2 μL of stock solutions of heavy atom compound to the drop containing the crystals for a final concentration of 0.5 mM of KAu(CN)₂.
- Data for a crystal grown in 0.06 M Divalents, 0.1 M Buffer System 1, 50 % v/v Precipitant Mix 4, were collected at beamline P11 of Petra III, DESY, Hamburg.
- The structure of OtCE15A was solved by molecular replacement using an unpublished structure of a bacterial CE15 from the same project, which shares 49.87% sequence identity with OtCE15A, at 1.49 Å resolution.

Structure of OtCE15A

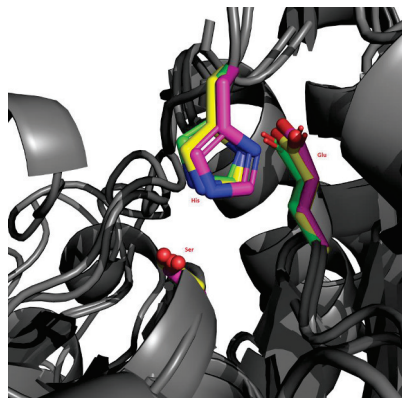
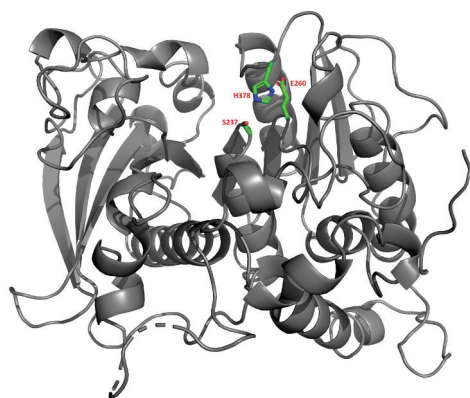


Figure 3:
Left: Overall structure of OtCE15A (not published) from bacterium *Opiritus terrae*. The β-sheet is positioned between two clusters of α-helices, with two β-strand antiparallel to the others, resulting in a twisted β-sheet. The catalytic triad is displayed as green sticks. Right: Close up of the catalytic triad Ser237-His378-Glu260 of bacterial OtCE15A (green) superpositioned on top of the catalytic triad of the two previously published GE structures of StGE2 (magenta, PDB: 4G4J and Cip2_GE (yellow, PDB: 3PIC). Picture made in Pymol.

- The structure has the typical α/β hydrolase fold
- The catalytic site of OtCE15A is proposed to be Ser237-Glu260-His378
- OtCE15A shows an extra loop at residue 111 (Phe) to 161 (Ala) compared to other CE15
- Comparison between OtCE15A with Cip2_GE (PDB: 3PIC) and StGE2 (PDB: 4G4G) shows that the catalytic triad is well preserved between fungi and bacteria throughout evolution.

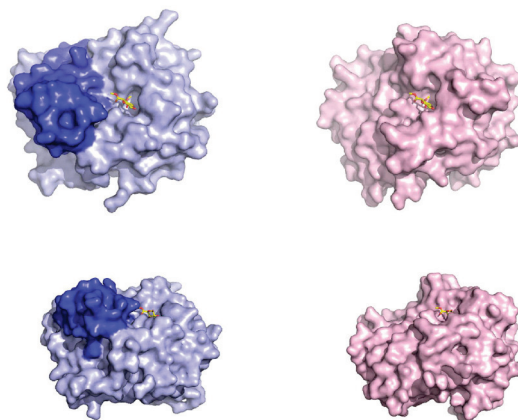


Figure 4: Top left: Top view of OtCE15A superimposed with 4G4J substrate. Top right: Top view of 4G4J. Bottom left: Side view of OtCE15A superimposed with substrate from 4G4J structure. Bottom right: Side view of 4G4J. Dark blue area indicates the extra loop at residue 111-161. 4G4J: StGE2 mutant (S213A) in complex with 4-O-methyl-β-D-glucopyranuronate. The ligand from 4G4J is shown in all four pictures. Picture made in Pymol

Catalytic activity

The activity of OtCE15A has been tested on a number of model substrates, indicating higher catalytic efficiency on benzyl glucuronate.

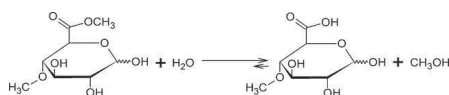


Figure 5:
Top: Reaction diagram showing the hydrolysis of methyl 4-O-Me-D-Glucopyranuronate by the fungal GE StGE2, PDB 4G4G [5].
Bottom: Activity measurements of OtCE15A on different model substrates.

OtA activity	K _m (mM)	Error	k _{cat} (s ⁻¹)	Error	K _{cat} /K _m ((s·M) ⁻¹)	Error
Benzyl glucuronate esterase activity	4.31	0.36	19.3	0.48	4.47·10 ³	3.88·10 ²
Methyl galacturonate esterase activity	5.74	0.22	10.7	0.11	1.87·10 ³	75.8
p- nitrophenol acetate esterase activity	Not Saturatable up to 10 mM				35.7	47

Crystallographic parameters and refinement statistics

Data collection	
Date	2017.08.27
Source	PETRA III p 11
Wavelength (Å)	0.979
Space group	P1
No of molecules in asym. Unit	1
Cell dimensions	
a, b, c (Å)	43.69, 44.61, 50.56
α, β, γ (°)	75.57, 66.17, 70.65
No. of measured reflections	180550 (28703)
No. of independent reflections	50802 (7975)
Resolution (Å)	46.27-1.50 (1.59-1.50)
R _{merge} (%)	4.2 (31.4)
R _{meas} (%)	5.0 (37.0)
CC(½)	99.9 (92.3)
I/σ	16.69 (3.40)
Completeness (%)	95.9 (93.3)
Redundancy	3.55 (3.60)
Refinement	
R _{work} /R _{free}	0.1349/0.1597
No. Atoms	
Protein	6302
Ligand/ions	77
Water	402
B-factors	
All atoms (Å ²)	26
Rmsd	
Bond lengths (Å)	0.008
Bond angles (°)	1.056

References

- [1] Blåth et al., FEBS Letters. Vol. 590(16), 2611-2618 (2016)
- [2] Li et al., FEBS Letters. Vol 581(21), 4029-4035 (2007)
- [3] d'Errico et al., Journal of Biotechnology. Vol. 219, 117-123 (2006)
- [4] Williamson et al., Scientific reports, Vol. 7: 17278 (2017)
- [5] Charavji et al., Acta Cryst. Vol. 69, 63-73 (2013)

Programs

- XDS (<http://ds.mpimf-heidelberg.mpg.de/>)
- Phenix (<https://www.phenix-online.org/>)
- COOT (<http://mb.bioch.ox.ac.uk/cool/>)
- Pymol (<http://www.pymol.org/>)

Thanks

- PETRA III
- Danish instrument Center DANSCATT





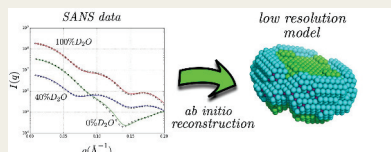
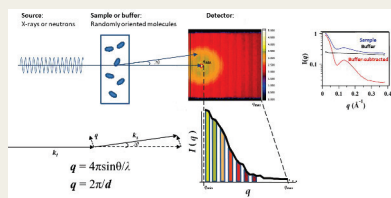
Sample area and detector tank of the Bio-SANS instrument at the High-Flux Isotope Reactor of Oak Ridge National Laboratory (Tennessee, USA).

Introduction. The genetic code of viruses is typically protected by a spherical protein container. This protein capsid is assembled from hundreds of individual proteins in a spontaneous self-assembly process. We currently lack a detailed structural model for how self-assembly proceeds from the isolated subunits into the final protein capsid and how RNA/DNA gets incorporated into the capsids. We aim to study the capsid assembly process of hepatitis B virus using time resolved Small-Angle Neutron Scattering (SANS). Assembly of capsid will be triggered by mixing of capsid building blocks and RNA and the reaction will be followed over time. Using solvent contrast matching the structural transitions in protein and RNA over time can be followed separately and this will give a unique insight into the capsid assembly pathway and the conformation of RNA. We specifically plan to study how the length of incorporated RNA affects the protein self-assembly pathway and how the structure of RNA changes during the assembly process. In parallel we develop computational methods to analyze the experimental data by combining kinetic modeling, structure-based scattering calculations and Bayesian statistical inference.

Small-angle scattering.

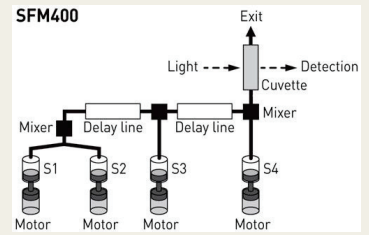
- Provides information about macromolecular size and shape
- Neutrons provide additional contrast-matching ability
- Capabilities are improving for smaller sample volumes and time-resolved

Measurements



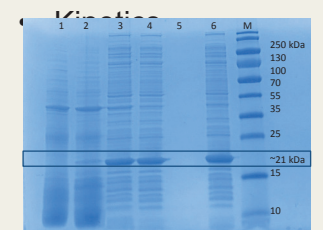
Sample Preparation.

- Capsid proteins forming virus-like particles expressed in *E. coli*
- Purified capsid proteins will be monitored with SANS during capsid formation



Schematic overview of stopped-flow mixing for time-resolved measurements. This process has been implemented at SANS2D of ISIS Neutron Source (Oxford, UK).

- Capsid formation will be initiated by the addition of RNA or assembly buffer



(1&2) *E. coli* cells, uninduced and induced with 1 mM IPTG overnight at 21 C. (3&4) Whole cell lysate and clarified lysate. (5&6) Ultracentrifugation supernatant and pellet after 14 hours at 120k x g. (M) Molecular weight marker

Data analysis.

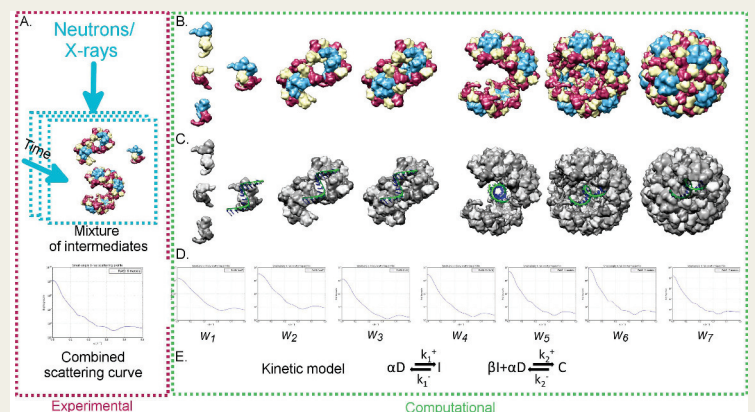
- Structure-based scattering calculations from experimental data and atomic models (PDB and Rosetta macromolecular software suite)
- Bayesian statistical inference used to determine concentration and weighting of multiple intermediate components during assembly
- Assembly pathway kinetics develops a model for protein self-assembly in viral capsid assembly

Progress / Future directions.

- 2 successful beamtime proposals (ORNL, ISIS)
- Purification being performed and optimized

¹Department of Biochemistry and Structural Biology, Lund University, Naturvetarvägen 14, 221 00, Lund, Sweden

²Preliminary computational methods in development
²European Spallation Source ERIC, Data Management and Software Center, Ole Maaløesvej 3, 2200 Copenhagen N, Denmark



- Experimental time-resolved scattering data for mixtures of intermediates are acquired (A)
- Scattering curves are simulated for each high-resolution model of protein (B) or nucleic acid (C)
- Based on these curves and experimental data a deconvolution algorithm determines the weights (D), which are coupled through a kinetic model (E)

Biochemical And Structural Investigation of the CE15 Family of Enzymes: Important Enzymes Acting To Liberate Hemi-cellulose from Lignin

Scott Mazurkewich^{ab}, Jenny Arnlind Bååth^{ab}, Jens-Christian Navarro Poulsen^c, Rasmus Meland Knudsen^c, Lisbeth Olsson^{ab}, Leila Lo Leggio^c and Johan Larsbrink^{ab}

^a Division of Industrial Biotechnology, Department of Biology and Biological Engineering, Chalmers University of Technology, Gothenburg, Sweden

^b Wallenberg Wood Science Center, Chalmers University of Technology, SE-412 96 Gothenburg, Sweden

^c Department of Chemistry, HC Ørsted's Institutet, Copenhagen University, Copenhagen, Denmark

Background

- Glucuronoyl esterases (GEs) are a relatively new class of enzymes which cleave an ester linkage connecting lignin to glucuronoyl xylan (Figure 1A).
- Putative GEs have now been identified in many biomass degrading microbes and the enzymes are now classified into the large Carbohydrate Esterase Family 15 (CE15).
- Phylogenetic analysis of CE15 members indicates that the family has a wide degree of sequence diversity (Figure 1B).
- To-date, only a few GEs have been biochemically characterized and only two protein structures, both from only one clade of the tree, have been determined.

Objective

- To advance our understanding of the CE15 family by biochemically characterizing and determining structures of bacterial CE15 proteins from across the protein family.

Methods

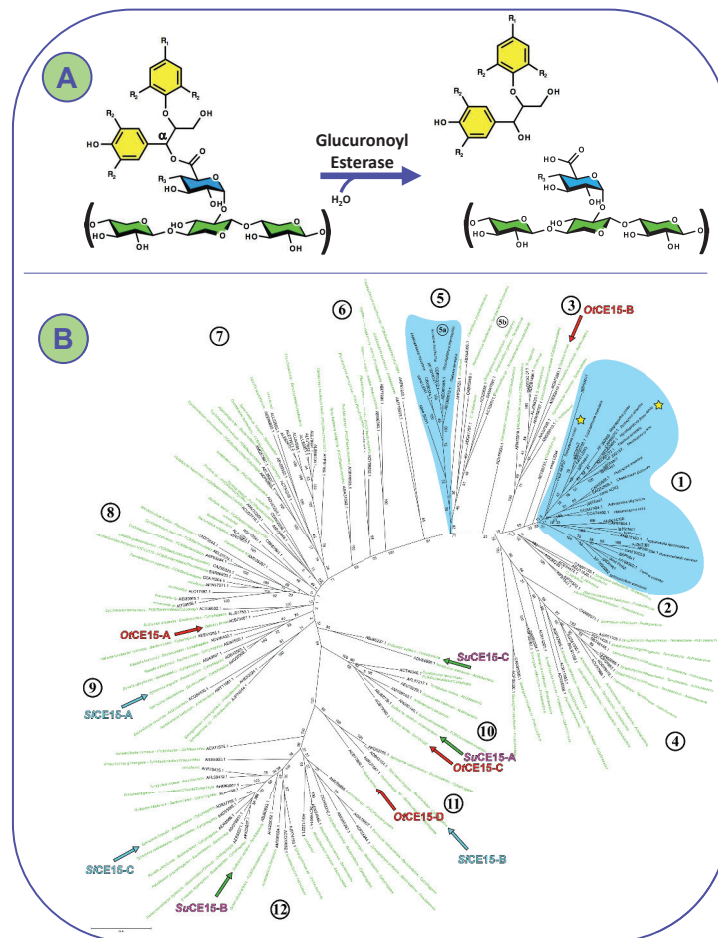
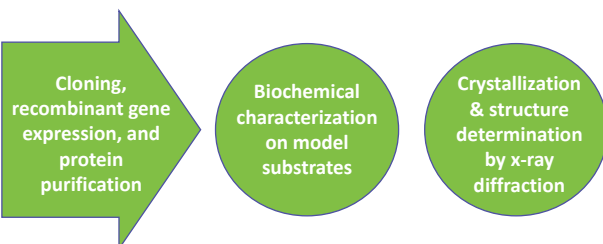


Figure 1: Glucuronoyl esterase reaction (A). GEs break the ester linkage between lignin (red) and glucuronic acid (blue) found on xylan chains (green). Phylogenetic analysis of CE15 family members found in the carbohydrate active enzyme (CAZy) database (B). Fungal CE15 proteins represent a small portion of the diversity and cluster into two defined clades (blue background). Whereas, CE15 members from bacterial origin are highly diverse (green text). Yellow stars indicate the gene records that have protein structures determined and arrows indicate CE15 proteins investigated here.

Biochemical Characterization

CE15	Clade	k_{cat}/K_m ($s^{-1}M^{-1}$)			
		Benzyl Glucuronate	Allyl Glucuronate	Methyl Glucuronate	Methyl Galacturonate
OtCE15-A	8	4.64×10^3	8.80×10^3	6.85×10^3	4.85×10^3
OtCE15-B	3	1.86×10^1	2.82	1.14	8.68
OtCE15-C	10	1.16×10^4	2.49×10^3	8.98×10^2	1.19×10^3
OtCE15-D	11	1.11×10^4	3.45×10^3	5.19×10^2	1.95×10^{-6}
SICE15-A	9	1.88×10^3	1.00×10^3	1.55×10^3	3.82×10^1
SICE15-B	12	2.60×10^3	9.08×10^2	4.57×10^2	3.66×10^{-7}
SICE15-C	12	9.69×10^2	1.11×10^2	1.03×10^2	3.73×10^{-6}
SuCE15-A	10	2.20×10^4	5.47×10^3	2.32×10^3	1.62×10^3
SuCE15-B	12	1.49×10^3	3.65×10^2	6.00×10^2	9.00×10^{-3}
SuCE15-C	10	2.27×10^4	1.57×10^4	1.66×10^4	1.59×10^3

Table 1: Catalytic efficiencies of CE15 enzymes investigated on model substrates. Means and standard errors of duplicate measurements are presented. **Not determined due to low activity

- All of the enzymes have glucuronoyl esterase activity.
- Many show minimal discrimination between small and large ester substituents (methyl vs phenyl).
- Enzymes from clades 11 and 12 discriminate between uronate substrates (Me-Glc vs Me-Gal).

Future Work

- Investigating hypothesized roles of active site residues.
- Co-crystallization of SuCE15-C with ligands.

Crystal Structure of SuCE15-C

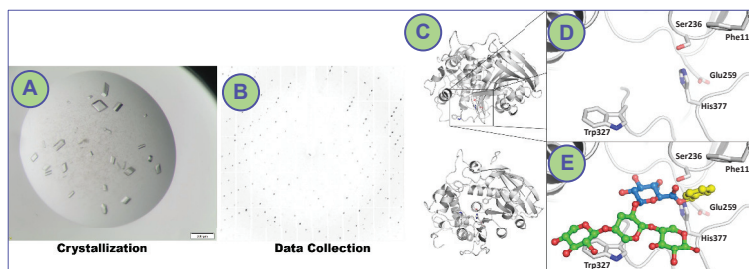


Figure 2: Structure of SuCE15-C. Crystals of SuCE15-C were produced by sitting drop from 23 mg/mL of protein with a condition from a Morpheus screen (A). X-ray diffraction image obtained from one of the crystals seen from panel A (B). Data were collected at beamline P11, Petra III, DESY, Hamburg. The structure was solved using isomorphous replacement from a selenomethionine substituted protein crystal. Overall structure of the enzyme (C). Close-up view of the proposed active showing putatively important residues (D). Proposed model of substrate, coloured as in figure 1, binding to the enzyme leading to catalysis (E).

- The overall fold is an $\alpha\beta\alpha$ -sandwich similar to the fungal CE15 proteins previously solved.
- Contains the catalytic triad (Glu-His-Ser) of serine hydrolases.
- Differences lie mostly on the surface of the protein leading to possible differences in substrate recognition.
- Modelling of a proposed glucuronoyl xylan into the active site has lead to hypothesized roles for specific residues.

Numerical Methods for 3D Inversion of Diffraction Patterns

Tiago Ramos^a, Martin Skovgaard Andersen^b, Jens W. Andreasen^a

^a Technical University of Denmark – Department of Energy Conversion and Storage, Roskilde, Denmark

^a Technical University of Denmark – Department of Applied Mathematics and Computer Science, Lyngby, Denmark

Abstract: The ability to image the nanoscale internal structure of numerous engineering and biological systems is considered to be a crucial tool for their study and understanding in order to promote further technological research and development. Coherent Diffraction (or Diffractive) Imaging (CDI) is an X-ray microscopy variant that does not rely on optical lenses and therefore has the ability to return higher spatial resolutions than the current numerical apertures for X-ray lenses. Here we present a numerical algorithm for 3D combined phase-retrieval and tomographic reconstruction of far-field coherent diffraction patterns. Our model supports the description of a 3D flexible projection geometry setup, which extends its application to large fields-of-view (ptychography) and allows the introduction of *tilts* and *translations* between the sample and detector for each acquired diffraction pattern.

Introduction: Three-dimensional phase-contrast imaging usually comprises three different successive steps: phase-retrieval, tomographic alignment and tomographic reconstruction. Phase-retrieval algorithms for coherent diffraction imaging are already well established in the literature but are limited to the reconstruction of a two-dimensional complex transmissivity function that is later used as a projection imaging in conventional tomographic reconstruction algorithms.

An exception to this traditional approach is the work done by Simon Maretzke and Tim Salditt [1] that successfully implemented a combined phase-retrieval and tomographic reconstruction for in-line holography measurements.

In our work, we generalized the *forward projector* operator, so that it accounts for limited fields-of-view on the sample and allows the introduction of additional degrees of freedom such as sample translations and tilts relative to the detector.

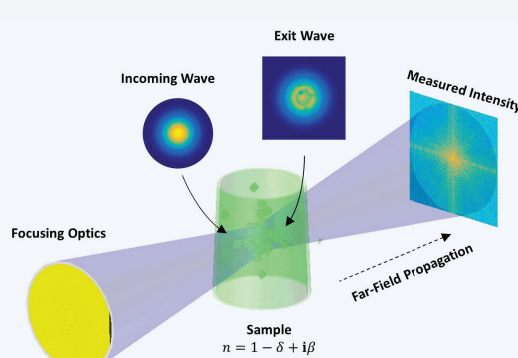
The combined phase-retrieval and tomographic reconstruction is framed as a non-linear inverse problem, solved by means of the Levenberg-Marquadt algorithm.

The *forward* and *backward* operators are GPU accelerated, assisted by the ASTRA toolbox [2], for faster computations on large datasets.

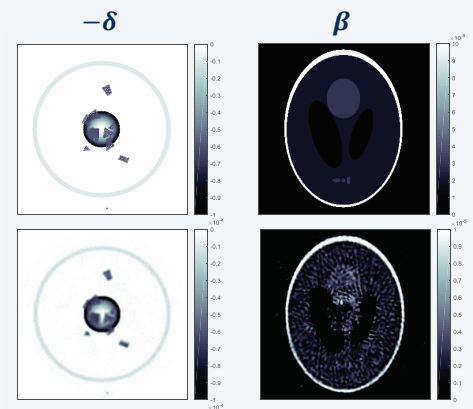
Methods: For a given sample described by its complex refractive index $n = 1 - \delta + i\beta$, the measured intensities in the X-ray detector are modelled according to

$$I^{\text{meas}} := \left| \mathcal{F} \left\{ P \exp \left[ik \int_{\Omega} -\delta + i\beta \right] \right\} \right|^2$$

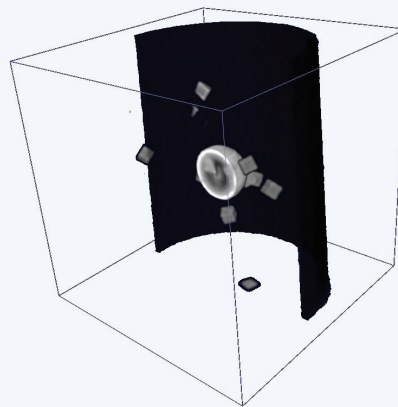
where \mathcal{F} represents the two-dimensional Fourier Transform operator, P the *probe function* and Ω the domain or field-of-view of the sample at each scanning coordinate.



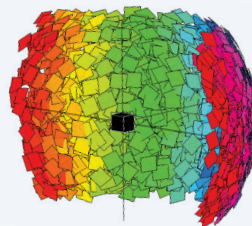
General Experimental Setup: Data acquisition in Scanning CDI. An incoming coherent parallel X-ray beam is focused in a region of interest of the sample. The incoming wavefield is attenuated and phase shifted according to the sample refractive index and further propagated to the detector plane (Far-field propagation = Fourier Transform).



Tomographic Reconstruction of simulated data: On the top: Central slices of the *sample phantom*, on the bottom: Central slices of reconstructed tomograms. The pixel intensities represent the real and imaginary decrement of the sample complex refractive index.



Preliminary reconstruction results: Sagittal cuts over reconstructed tomogram. On the left: real decrement of refractive index related to the sample scattering power; on the right: imaginary decrement of refractive index related to the sample absorption. These reconstructions were obtained after 6 iterations of the Levenberg-Marquadt algorithm for a total of 2880 diffraction patterns with dimensions 100x100 Pixels. Weakly absorbing samples result in poor reconstructions of the imaginary part of the refractive index.



Flexible Projector Geometry: Besides its GPU implementation, for fast computations, the ASTRA toolbox is specially convenient to define more general projection geometries. The tomographic reconstructions here presented resulted from simulated diffraction patterns acquired at random orientations as illustrated above.

Acknowledgements: We would like to acknowledge Simon Maretzke and Tim Salditt for their previous related work in in-line holography (near-field) that served as a solid inspiration and starting point for our current research.

References:

- [1] S. Maretzke, M. Bartels, M. Krenkel, T. Salditt, and T. Hohage, "Regularized Newton Methods for X-ray Phase Contrast and General Imaging Problems," vol. 344, no. 1999, pp. 40–55, 2015.
- [2] W. van Aarle et al., "The ASTRA Toolbox: A platform for advanced algorithm development in electron tomography," *Ultramicroscopy*, vol. 157, pp. 35–47, 2015.



Multi-phase 3D Image Segmentation with Tetrahedral Mesh



Tuan Nguyen

DTU Compute, Technical University of Denmark
tntnr@dtu.dk

Abstract

We propose a method for 3D image segmentation using tetrahedral mesh. Our model is a deformable model that deforms the mesh to capture the segmenting regions. The advantages of our method are: multi-phase segmentation; output is a tetrahedral mesh.

1. Motivation

Segmentation of CT scan is an important tool for material analysis. Generally, the segmentation can be represented using implicit representations (e.g. the level set) or explicit representations (e.g. tetrahedral mesh). Among these two, explicit representations show more advantages for analysis:

- It is easier to measure quantitative information (surface area, curvature, etc.)
- Ready for simulation like FEM

Traditional approaches to obtain a 3D explicit segmentations usually consist of two steps: First segment individual 2D slice with implicit representation; and then generate a tetrahedral mesh from these 2D segmentation. This procedure takes time and reduce the accuracy of the segmentation (Fig. 1).

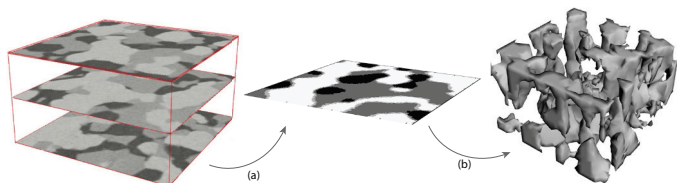


Figure 1: Traditional approach. (a) 2D segmentation of individual slice (b) Surface/domain mesh generation

In our approach, we segment 3D image using a tetrahedral mesh directly. The advantages of our method include: Multi-phase segmentation, output is a tetrahedral mesh, and higher accuracy.

2. Approach

Segmentation representation: We label the tetrahedra to the material they belong to. Triangles (faces), whose co-boundary tetrahedra have different labels, define the surface. The unknown we need to solve is the surface vertex positions and the labeling function.

Dynamics model: We utilize deformable model (active contour) that deforms the mesh iteratively to capture the segment, and it helps our method be strong to noise and artifact [2]. We derive the deformation forces by minimizing the Mumford-Shah [1] energy function.

$$E = \int_{\Omega} (I - g)^2 d\Omega + \alpha \text{Area}(\Gamma) \quad (1)$$

An example of deforming mesh in 2D is shown in Fig. 2.

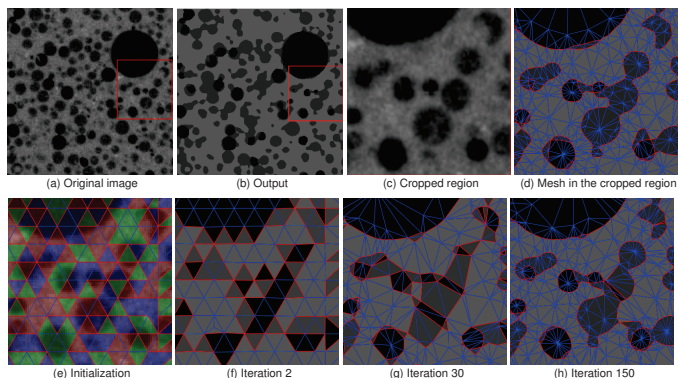


Figure 2: Evolution of the mesh. Top row: Original image and segmentation; Bottom row: evolution of the mesh

5. Segmentation tool

We are planning to make our method available to public.

- C++ source code
- Binary executable
- Possible to run on the miGrid or any cluster server

6. Future works

We are implementing adaptive resolution mesh for optimal representation of the mesh.

References

3. Intensity based segmentation

Fig. 3 shows the segmentation using the image intensity as the input. All the segmentations contain three phases, but our method can handle arbitrary number of phases.

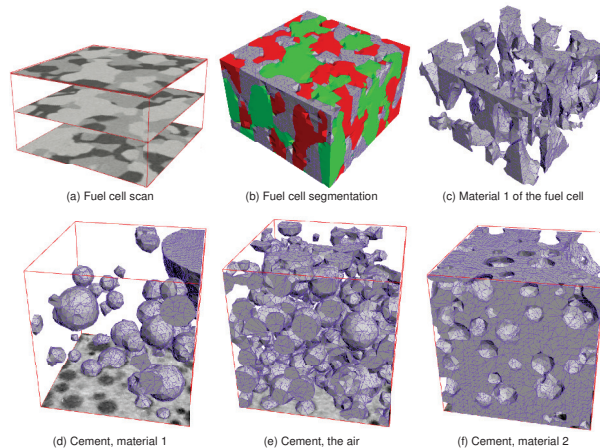


Figure 3: 3D segmentations of fuel cell (top row) and cement (bottom row)

4. Probability input

The input of our method can be flexible. Fig. 4 shows an example where pure intensity could not distinguish the orientations of the carbon fiber bundles. By applying an orientation filter, we obtain the probability maps. The probability maps can be used as input to our method.

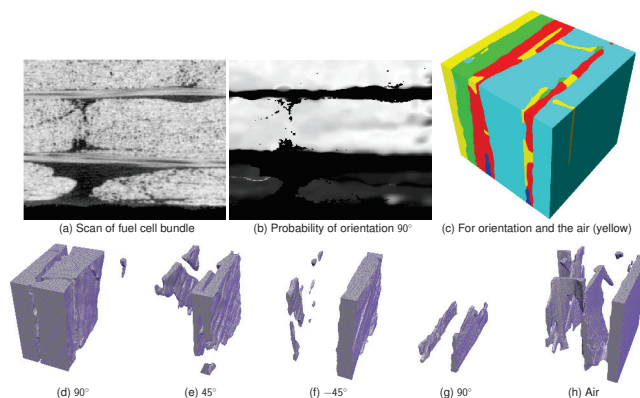


Figure 4: Segmentation using orientation filter

Fig. 5 shows another example, where we use probability from dictionary method as the input.



Figure 5: Segmentations use patch similarity

[1] David Mumford and Jayant Shah. Optimal approximations by piecewise smooth functions and associated variational problems. *Communications on Pure and Applied Mathematics*, 42, 1989.

[2] Chenyang Xu, Jerry L Prince, and Dzung L. Pham. Image Segmentation Using Deformable Models. In *Handbook of Medical Imaging*, pages 129–174. 2004.



LUND UNIVERSITY

LP3 & DEMAX

Wolfgang Knecht¹, Claes von Wachenfeldt¹ & Zoë Fisher^{1,2}

¹Lund Protein Production Platform (LP3), Sölvegatan 35, 22362 Lund, Sweden and ²Scientific Activities Division, European Spallation Source ERIC (ESS), Tunavägen 24, 22100 Lund, Sweden.

Proteins are of enormous importance to life on earth and have a multitude of different functions in all organisms. They can work as enzymes, gene regulators, structural components, transporters, and receptors. In disease, most drugs act on proteins. It is therefore unsurprising that the structures and mechanisms of proteins are prominent topics in life science research.

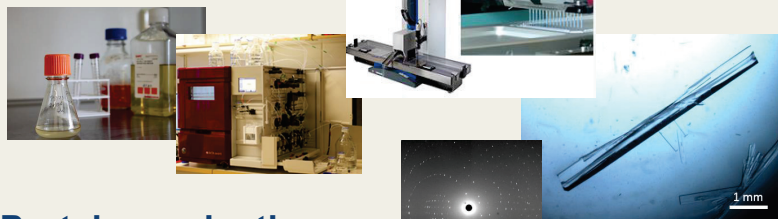
Access to both state-of-the-art X-ray (MAX IV) and neutron sources (ESS) will increase the capacity for innovation in the life sciences in Lund. To enable efficient use of these unique and powerful facilities by Lund researchers, Lund University hosts the Protein Production Platform, **LP3** (www.lu.se/lp3).

The DEuteration and MAcromolecular Xtallization (DEMAX) platform of the European Spallation Source ERIC (ESS) co-localized with LP3 in 2016.



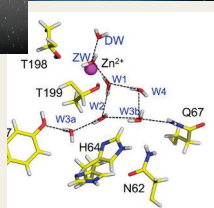
LP3 and DEMAX are located in the Biology building A, Sölvegatan 35, Lund, Sweden. (lp3@biol.lu.se, www.lu.se/lp3), close to the sites for MAX IV and ESS.

LP3 can help with:



Protein production

- Plasmids for protein production
- Recombinant protein production:
 - a. in bacteria (*E. coli*)
 - b. in eukaryotic (insect) cells
- Protein labeling with stable isotopes (2H, 13C, 15N)
- Protein purification



High-throughput crystallization

LP3 can carry out sample characterization and a wide variety of nano-volume robot-assisted crystallization experiments with:

- SEC, DSF and DLS
- Mosquito nanolitre pipetting robot with LCP
- UV imaging system with plate hotel

Structure determination

- Applications for beamtime at synchrotron facilities
- Collect and process x-ray data

Bio-deuteration

In neutron macromolecular crystallography production of deuterated proteins is critical. The incoherent neutron scattering from hydrogen generates a high background that can be reduced by replacing hydrogen with deuterium. DEMAX and LP3 are coordinating in their efforts to develop cost-effective methods for:

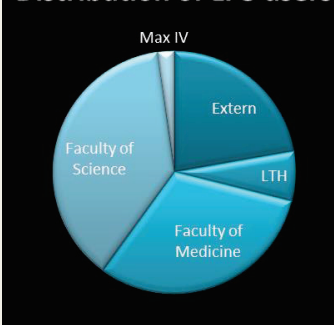
- Production of deuterated proteins for macromolecular crystallography
- Crystallization of interesting proteins for neutron work
- Production of labeled proteins/lipids for neutron reflectometry.

For further information: www.lu.se/lp3

Brief Facts 2017

45 users | 91 unique deliveries in 53 protein production projects | 158 protein crystallization plates | 10 visitors at LP3

Distribution of LP3 users



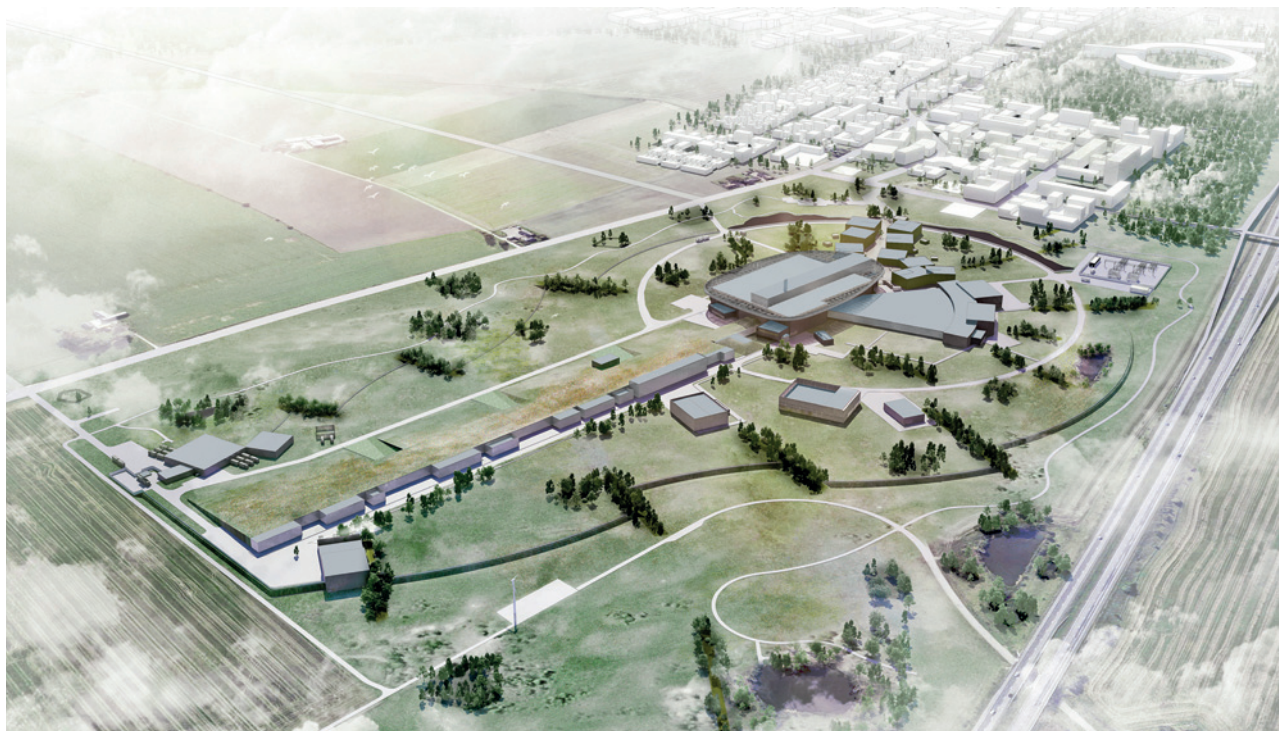
Registered participants for the MAX4ESSFUN Annual Meeting 2018

Name	Mail	Organization
Aleksandar Matic	matic@chalmers.se	Chalmers
Alessandra Zarantonello	azara@mbg.au.dk	Aarhus University
Alexander Svanbergsson	alexander.svanbergsson@med.lu.se	Lund University
Anan Yaghmur	anan.yaghmur@sund.ku.dk	University of Copenhagen
Anders Bjorholm Dahl	abda@dtu.dk	DTU
Anders Madsen	anders.madsen@xfel.eu	Other
Anders Malmström	anders.malmstrom@med.lu.se	Lund University
Andressa de Zawadzki	andressa@food.ku.dk	University of Copenhagen
Andrew Cassidy	amc@phys.au.dk	Aarhus University
Anja Schmidt-Christensen	anja.schmidt-christensen@med.lu.se	Lund University
Ann Terry	ann.terry@maxiv.lu.se	MAX IV
Anna Hjerresen Schuppli	anhs@implement.dk	University of Copenhagen
Antoni Kowalski	antoni.kowalski@mbg.au.dk	Aarhus University
Artur Glavic	artur.glavic@psi.ch	Other
Carl Malm	carl.malm@innovationskane.com	Other
Celine Durniak	celine.durniak@esss.se	ESS
Christian Rein	chrr@dtu.dk	DTU
Claes von Wachenfeldt	claes.von_wachenfeldt@biol.lu.se	Lund University
Dan Holmberg	dan.holmberg@med.lu.se	Lund University
Dan Krska	krska@chalmers.se	Chalmers
Deepak Jain	deepak.jain@med.lu.se	Lund University
Di Lu	di.lu@physics.gu.se	University of Gothenburg
Dirk Mütter	mueter@nano.ku.dk	University of Copenhagen
Dmitri Mitcov	mitcov@chem.ku.dk	University of Copenhagen
Edzard Spillner	e.spillner@eng.au.dk	Aarhus University
Elis Sjögren	elis.sjogren@material.lth.se	Lund University
Elisabeth Josten	e.josten@fz-juelich.de	Other
Emil Tykesson	emil.tykesson@med.lu.se	Lund University
Erika Tudisco	erika.tudisco@construction.lth.se	Lund University
Eskil Mårtensson	eskil.martensson@skane.se	Other
Esko Oksanen	esko.oksanen@esss.se	ESS
Florian Schmitz	florian.schmitz@gu.se	University of Gothenburg
Folmer Fredslund	folf@biosustain.dtu.dk	DTU
Frederic Jabs	jabs@eng.au.dk	Aarhus University
Frederik Gjørup	fgjorup@chem.au.dk	Aarhus University
Georgios N. Kalantzopoulos	georgiok@smn.uio.no	University of Oslo
Gergely Nagy	nagy.gergely@wigner.mta.hu	ESS
Giovanni Fevola	gfev@dtu.dk	DTU
Gregers Rom Andersen	gra@mbg.au.dk	Aarhus University
Hans Martin Kjer	hmkj@dtu.dk	DTU
Hazel Reardon	hazel@inano.au.dk	Aarhus University
Heidi Asschenfeldt Ernst	hae@chem.ku.dk	University of Copenhagen
Heidi Døring	heidi@chem.ku.dk	University of Copenhagen
Helen Yu	helen.yu@jur.ku.dk	University of Copenhagen
Helle Juel Martens	hjm@plen.ku.dk	University of Copenhagen

Helmer Fjellvåg	helmer.fjellvag@kjemi.uio.no	University of Oslo
Ida Gjerlevsen Nielsen	idagn@chem.au.dk	Aarhus University
Jacob Becker	jbecker@chem.au.dk	Aarhus University
Jakob Øster	jakob.oester@regionh.dk	The Capital Region of Denmark
Jens Preben Morth	j.p.morth@ncmm.uio.no	University of Oslo
Jens Wenzel Andreasen	jewa@dtu.dk	DTU
Jeppe Baden	Jeppe@chem.ku.dk	University of Copenhagen
Johan Bergenholtz	jbergen@chem.gu.se	University of Gothenburg
Johan Engblom	johan.engblom@mau.se	Malmö University
Johan Larsbrink	johan.larsbrink@chalmers.se	Chalmers
John H. Ipsen	ipsen@memphys.sdu.dk	Other
Jonas L. Bertelsen	s134281@student.dtu.dk	DTU
Jonatan Wårdh	jonatan.wardh@physics.gu.se	University of Gothenburg
José Xavier Sierra Trujillo	jxst@dtu.dk	DTU
Julie Winkel Missel	juliem@sund.ku.dk	University of Copenhagen
Kajsa Paulsson	kajsa_m.paulsson@med.lu.se	Lund University
Karin Sahlin	karin.sahlin@chalmers.se	Chalmers
Kasper Pedersen	kastp@kemi.dtu.dk	DTU
Kasper Skov Kjær	kaspersk@gmail.com	Lund University
Katarina Koruza	katarina.koruza@biol.lu.se	Lund University
Kathryn Browning	kathryn.browning@sund.ku.dk	University of Copenhagen
Kell Mortensen	kell@nbi.dk	University of Copenhagen
Kenneth Holm-Dahlin		Other
Kim Krighaar Rasmussen	KKR@chem.ku.dk	University of Copenhagen
Kim Lefmann	lefmann@nbi.ku.dk	University of Copenhagen
Konstantin Klementiev	konstantin.klementiev@maxiv.lu.se	MAX IV
Kristina Hedfalk	kristina.hedfalk@gu.se	University of Gothenburg
Kaare Bjerregaard-Andersen	kaarebj@kjemi.uio.no	University of Oslo
Lasse Rabøl Jørgensen	lasserj@chem.au.dk	Aarhus University
Leila Lo Leggio	leila@chem.ku.dk	University of Copenhagen
Linda Udby	udby@nbi.dk	University of Copenhagen
Lise Ørdukl Sandberg	lise.sandberg@nbi.ku.dk	University of Copenhagen
Liv Sofia Elinor Damgaard	pnh136@alumni.ku.dk	University of Copenhagen
Luise Theil Kuhn	luku@dtu.dk	DTU
Mads Bertelsen	mads.bertelsen@gmail.com	University of Copenhagen
Manish Singh	manish.singh.itbh06@gmail.com	Lund University
Marcella Berg	marcellac.berg@gmail.com	University of Copenhagen
Maria Gourdon	maria.gourdon@biol.lu.se	Lund University
Mariam Andersson	maande@dtu.dk	DTU
Marite Cardenas	marite.cardenas@mah.se	Malmö University
Mariusz Kubus	makub@kemi.dtu.dk	Other
Marjolein Thunnissen	marjolein.thunnissen@maxiv.lu.se	MAX IV
Martin Bech	martin.bech@med.lu.se	Lund University
Martin Meedom Nielsen	mmee@fysik.dtu.dk	DTU
Mathias Kjærgaard Christensen	mkch@dtu.dk	DTU
Mathias Mikkelsen	ljt123@alumni.ku.dk	University of Copenhagen
Mathias Mørch	mmorch@chem.au.dk	Aarhus University

Maths Karlsson	maths.karlsson@chalmers.se	Chalmers
Mats Granath	mats.granath@gu.se	University of Gothenburg
Matthias Amann	matthias.amann@kjemi.uio.no	University of Oslo
Matti Knaapila	matti.knaapila@fysik.dtu.dk	DTU
Mei Lee Ling	meilee.ling@inano.au.dk	Aarhus University
Michael Gajhede	mig@sund.ku.dk	University of Copenhagen
Michael Korning Sørensen	michaelkorning@gmail.com	DTU
Mika Torkkeli	mtork@fysik.dtu.dk	DTU
Milda Pucetaite	milda.pucetaite@cec.lu.se	Lund University
Mirja Carlsson Möller	mirja.carlsson_moller@maxiv.lu.se	MAX IV
Monica Jane Emerson	monj@dtu.dk	DTU
Nadia Glæsner	nagl@plen.ku.dk	University of Copenhagen
Naseem Abdel	naseem.abdel77@gmail.com	Other
Neelima Kandula	neelima.kandula@geo.uio.no	University of Oslo
Nicolai André Brogaard Riis	nabr@dtu.dk	DTU
Niels Bøgholm	nb@mbg.au.dk	Aarhus University
Pascale Deen	pascale.deen@esss.se	ESS
Pernille Sønderby	perso@kemi.dtu.dk	DTU
Peter Stanley Jørgensen	psjq@dtu.dk	DTU
Poul Erik Lindelof	lindelof@it.dk	University of Copenhagen
Poul Norby	pnor@dtu.dk	DTU
Rasmus Meland Knudsen	thw934@alumni.ku.dk	University of Copenhagen
Reidar Lund	reidar.lund@kjemi.uio.no;	University of Oslo
Robin Woracek	robin.woracek@esss.se	ESS
Ryan Oliver	ryan.oliver@biochemistry.lu.se	Lund University
Salvatore De Angelis	sdea@dtu.dk	DTU
Sander Bruun	Sab@plen.ku.dk	University of Copenhagen
Sandra Cuellar Baena	sandra.cuellar-baena@maxiv.lu.se	MAX IV
Sara Malekkhayat Häffner	sara.malekkhayat-haffner@sund.ku.dk	University of Copenhagen
Scott Mazurkewich	Scott.Mazurkewich@chalmers.se	Chalmers
Sheng Guo	sheng.guo@chalmers.se	Chalmers
Shilova Anastasiia	Anastasiia.Shilova@maxiv.lu.se	MAX IV
Sindra Petersson Årsköld	sindra.petersson@esss.se	ESS (European Spallation Source)
Sofie Janas	sofie.janas@nbi.ku.dk	University of Copenhagen
Somrita Dhar	sodh@dtu.dk	DTU
Sonja Holm-Dahlin	sonjaholmdahlin@gmail.com	Aarhus University
Sophie Le Cann	sophie.le_cann@bme.lth.se	Lund University
Stacey Sørensen	Stacey.sorensen@sljus.lu.se	Lund University
Stergios Piligkos	piligkos@chem.ku.dk	University of Copenhagen
Steve Hall	stephen.hall@solid.lth.se	Lund University
Saara Laulumaa	saara.laulumaa@sund.ku.dk	University of Copenhagen
Therese Nordström	therese.nordstrom@mah.se	Malmö University
Thomas Ursby	thomas.ursby@maxiv.lu.se	MAX IV
Tiago Ramos	tiagoj@dtu.dk	DTU
Tomas Sigfrido Plivelic	tomas.plivelic@maxiv.lu.se	MAX IV
Tuan Nguyen	tntr@dtu.dk	DTU
Ulf Johansson	ulf.johansson@maxiv.lu.se	MAX IV

Ulf Molich	ulfmol@kemi.dtu.dk	DTU
Ulf Olsson	ulf.olsson@fkem1.lu.se	Lund University
Uwe Mueller	uwe.muller@maxiv.lu.se	MAX IV
Vinardas Kelpas	vinardas.kelpas@biol.lu.se	Lund University
Wolfgang Knecht	wolfgang.knecht@biol.lu.se	Lund University
Xiaodan Zhang	xzha@mek.dtu.dk	DTU
Zoe Fisher	zoe.fisher@esss.se	ESS



European Spallation Source ERIC



MAX IV synchrotron radiation laboratory